Ductile fracture of high strength steels with morphological anisotropy. Part I: Characterization, testing, and void nucleation law

Matthieu Marteleur[a], Julien Leclerc[b], Marie-Stéphane Colla[a], Van-Dung Nguyen[b], Ludovic Noels[b,*], Thomas Pardoen[a]

[a] *Institute of Mechanics, Materials and Civil Engineering, UCLouvain, B-1348 Louvain-la-Neuve, Belgium*
[b] *Computational & Multiscale Mechanics of Materials (CM3) Department of Aerospace and Mechanical Engineering, University of Liège, B-4000 Liège, Belgium*

Abstract

The ductile fracture behavior of a high strength steel is investigated using a micromechanics-based approach with the objective to build a predictive framework for the fracture strain and crack propagation under different loading conditions. Part I of this study describes the experimental results and the determination of the elastoplastic behavior and damage nucleation under different stress triaxiality and Lode parameter. The damage mechanism starts early void nucleation from elongated inclusions, either by particle cracking under loading oriented along the major axis, or by matrix decohesion when the main loading is transverse. Void nucleation is followed by plastic growth and coalescence. The long inclusion axis is preferentially aligned in one direction leading to significant failure anisotropy with the fracture strain in the transverse direction being almost 50% lower compared to the longitudinal one, even though the plastic behavior is isotropic. The experimental data are first used to calibrate the elastoplastic model. An enhanced anisotropic nucleation model is then developed and integrated into the Gurson-Tvergaard-Needleman scheme. The parameters identification of the anisotropic nucleation model is finally performed and validated towards the experimental results. All these elements are subsequently used in Part II to simulate the full failure behavior of all testing specimens in the entire spectrum of stress states, from nucleation to final failure.

Keywords: Ductile fracture, Gurson model, anisotropic nucleation

1. Introduction

Ductile fracture is the ubiquitous failure scenario occurring in metallic materials. It has been extensively addressed not only by experiments but also by theoretical studies, see the reviews in [1, 2, 3] and references therein. This fracture process occurs in multiple steps involving the nucleation, growth, and coalescence of voids, together with extensive plastic dissipation before final failure. Under macroscopic loading conditions, the fracture

*Corresponding author, Phone: +32 4 366 48 26, Fax: +32 4 366 95 05
Email address: L.Noels@ulg.ac.be (Ludovic Noels)

process starts when micro-cavities nucleate from cracking and/or debonding of the inclusions embedded in the metallic matrix. These micro-cavities grow and change shape through plastic deformation. Finally, in the last stage, the voids coalesce, resulting in cracking initiation followed by crack tearing.

In metallic alloys, there are four main sources of voids. First, cavities may pre-exist from manufacturing, leading to an initial porosity noted f_{V0}. In many commercial metals, f_{V0} is very small. The two main origins of voids are related to the presence of second phase particles. Voids can nucleate by either particle fracture or particle decohesion. These two mechanisms have been widely investigated, see reviews [4, 5, 6, 7, 3]. Void nucleation can occur early in the deformation process during the elastic loading or after minute amounts of plasticity, or sometimes only at very large deformation. Usually, small particles, typically in the submicrometer range, involving statistically less and smaller internal and interface defects, exhibit late nucleation, while large brittle particles often lead to early void nucleation. The void nucleation mode depends on the shape of the particles as well. Elongated particle tend to fragment when loaded parallel to the main loading axis, while showing decohesion when loaded transversally. The mode of nucleation depends also on the hardening law of the matrix, e.g. [8]. Void nucleation has been treated using phenomenological models relating the void nucleation rate $\dot{f}_{V\mathrm{nu}}$ (i.e. rate of void volume fraction production through nucleation) to the overall equivalent plastic strain rate or to the overall equivalent and hydrostatic stress rates. These laws, as formulated by Chu and Needleman [9], take into account a spread of the void nucleation events over the loading through a Gaussian distribution, allowing a maximum porosity f_n to be nucleated. The maximum porosity f_n is directly connected to the volume fraction of particles, with some complications arising in the case of particle fracture due to the original penny shape of the voids, e.g. [10, 11]. Other models directly relate the nucleation condition to the local stress and strain inside and at the interface of the particle and involve the famous work by the Beremin group [12], relying on homogenization theory. As a fourth source of voids, cavities can nucleate by accumulation of dislocations in some specific systems (e.g. in some hexagonal metals) or by accumulation of vacancies, favored for instance by irradiation and/or heating.

The mechanism void growth and coalescence are highly dependent on the stress state through the stress triaxiality, *i.e.* ratio of the hydrostatic pressure over the von Mises equivalent stress, and through the Lode parameter, which relates to the third invariant of the deviatoric stress tensor, as demonstrated through numerous researches in the literature, see *e.g.* the works [13, 14, 15, 16, 17, 18, 19, 20, 21, 22, 23, 24]. A high stress triaxiality leads to large void growth rates and fracture occurs mainly by internal necking of the ligaments between neighboring voids. At lower stress triaxiality, the voids tend to elongate and rotate while the porosity increases more slowly with plastic deformation. The Lode parameter plays an important role, and the fracture occurs sometimes with the formation of micro shear bands inclined to the main loading direction and joining primary voids, possibly with secondary voids nucleating inside these micro bands ("coalescence" in shear also called "void sheeting"). In the former case, the ductile fracture process is mainly governed by the stress triaxiality and the effect of the Lode parameter can be neglected whereas both the stress triaxiality and the Lode parameter considerably affect the latter [3]. The shear coalescence mechanism often leads to a slant crack propagation mode. Since metallic structures in engineering applications generally undergo complex stress states, a proper account of the stress state on the ductile

fracture process is mandatory for structural design, which in turn, constrains the material processing and development.

A large number of predictive computational models has been developed in the literature to combine an elastoplastic constitutive description of the metallic matrix with the evolution of the embedded voids. Probably the most common model is the Gurson model [25] in which a volume fraction of spherical voids is taken into account in the macroscopic yield criterion. This original model can only predict the void growth phase. It was subsequently extended in a semi-phenomenological form by Tvergaard and Needleman [26, 27], the so-called the GTN model, in order to take into account the void nucleation and void coalescence phases. The limitation of the GTN model in predicting failure under low stress triaxiality was partly resolved by introducing void shape effects [28, 29, 30] and partly, in [16], by incorporating a Lode-dependent heuristic term in the void evolution. Many other extensions of the GTN model have been proposed as reviewed in [1, 2, 3] and summarized hereafter for the one specifically used in the present study.

Although the GTN model and its extensions provide a complete computational methodology for the ductile fracture process, its description of the void nucleation process remains relatively empirical, missing a more in depth analysis of the phenomena at the inclusion level. An attempt is made in the present study to use a micromechanics-based model derived from the Beremin criterion [12], in which nucleation of voids starts when the critical stress at the inclusions is attained.

Furthermore, the phenomenological description of void coalescence, in which the porosity growth rate is artificially accelerated beyond a critical value of the porosity corresponding to the onset of coalescence, does not provide a realistic description of the void coalescence mechanism [13]. To better represent the coalescence process, micromechanics-based coalescence models pioneered in [31, 32] and further extended, see *e.g* the works [13, 33, 34, 35], the so-called Thomason model, have been addressed under the argument that coalescence corresponds to a localized plastic deformation in the ligaments between neighboring voids. The Thomason model can be used either to detect the onset of void coalescence while using the GTN framework [36], or as an additional yield surface competing with the GTN yield locus to govern the coalescence process (the so-called GTN/Thomason model) [13, 37, 38, 39]. The Thomason model is also used to govern the void coalescence process in the context of the multi-surface model [24].

Whenever the material degradation is modeled using a local constitutive model, the related boundary value problem becomes ill-posed during the material softening and the finite element solution becomes mesh-dependent [40]. This issue can be resolved using the implicit gradient enhanced nonlocal model pioneered in [41], see *e.g.* [42, 43, 44] when using the GTN model alone or [39, 24] when coupling the GTN and the Thomason models. Alongside the coupled GTN/Thomason model, the damage-to-crack transition framework is considered in [39], in which the crack surfaces are introduced in the mechanical problem through a cohesive band model during void coalescence.

Although ductile fracture of metals is an old field of research which may seem now mature, the number of studies combining advanced micromechanical models with enhanced void coalescence models expressed within a rigorous nonlocal formulation and well validated nucleation laws, and relying on a wide experimental basis are rarely found in recent literature.

The aim of this work is to apply the approach on a high-strength steel showing significant

morphological anisotropy under different stress states and loading directions through experimental and numerical analyses. The GTN/Thomason model under finite strains coupled with the implicit gradient enhanced nonlocal model and with the damage-to-crack transition framework recently developed in [39] is considered and validated using experimental results. The research is divided into two parts:

- In Part I, the experimental study based on a wide range of monotonic tensile tests under different stress states combined with microstructure and damage characterization is presented. The focus is on the identification of the elastoplastic behavior and on the stress triaxiality and the Lode effects on the void nucleation and fracture mechanisms. A new micromechanics-based void nucleation law enhancing the Beremin model [12] is then developed to capture the failure anisotropy emerging from the void nucleation process. Since the parameters identification of the nucleation law relies only on the microstructure characterization and on the void nucleation stage at low strains, we are already borrowing from Part II the calibrated version of the GTN model to validate this part of the work.

- In Part II [45], the calibration of the remaining parameters of the coupled GTN/Thomason model is investigated using void cell simulations and experimental results from Part I. Once all constitutive parameters are available, all the tests are simulated in order to assess the validity of the model. The damage-to-crack transition framework [39] is then applied to model the full crack propagation process.

Part I is organized as follows. The conducted experimental campaign is described in Section 2 and its results are analyzed in Section 3. The tensile tests are performed with different specimen types including smooth and notched round bars, plane strain specimens, and plane stress specimens in order to cover a wide range of stress triaxiality and Lode parameter. The cylindrical round bars are extracted from a large piece in the different directions to address the material anisotropy. In Section 4, the elastoplastic material parameters are identified and numerical simulations are performed to estimate the effect of the stress state on the fracture strain. In Section 5, an anisotropic void nucleation model is derived from reference [12] and integrated into the GTN model. The parameters identification of this anisotropic void nucleation model is performed and the numerical simulations show that the model can capture the effect of morphological anisotropy on damage evolution.

2. Experimental procedures

2.1. Material

The high strength steel (HSS) was received as hot forged hollow cylindrical pieces, see Fig. 1. These cylinders were water quenched after hot forging. Microstructural analysis of samples taken at various locations in the cylinders did not show heterogeneities along the thickness length. Figures 2a and 2b show scanning electron microscopy (SEM) images of the microstructure respectively perpendicular to the axis of the cylinder and to the radial direction. Black elongated precipitates are observed along the $z-r$ plane, showing a circular section in the $r-\theta$ plane. These precipitates are identified as MnS inclusions as commonly observed in industrial steels. The length of the inclusions ranges from a few up to 100

μm, with a mean diameter of 2 μm. A particle volume fraction of 2×10^{-3} is estimated from the surface fraction. Inserts in Figs. 2a and 2b highlight a martensitic microstructure after etching in Nital. XRD analysis showed no trace of residual austenite, as well as no crystallographic texture in the cylinders.

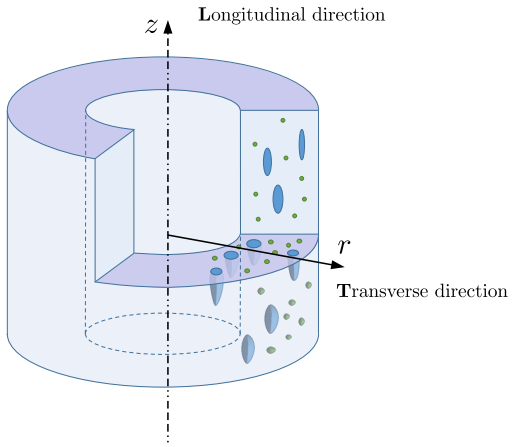

Figure 1: Schematic representation of the inclusion populations in the HSS material. Elongated inclusions aligned along the tube axis correspond to MnS precipitates and second family consists of small spherical carbide particles.

High magnification characterization of the microstructure highlights the presence of numerous carbides homogeneously dispersed inside the martensitic matrix, as illustrated in Fig. 2c. Their mean diameter is equal to $60 \pm 20nm$ and the volume fraction is about 7%.

Figure 1 is a schematic representation of the inclusion population in the HSS. The first population consists of large elongated inclusions aligned along the tube axis corresponding to MnS precipitates and the second population consists of small spherical carbide particles. In addition, the longitudinal and transverse directions are designated to refer respectively to the tube axis and circumferential directions.

2.2. Mechanical tests

All samples were cut by electric discharge machining (EDM) in order to avoid local heating and/or hardening of the material. The various geometries have been chosen in order to assess the influence of the loading conditions and directions on the failure of the material. The specimens were extracted from a forged tube, see Fig. 1 along both the longitudinal and transverse directions.

Three different types of geometry are tested including cylindrical round bars (denominated by RB), plane strain specimens (denominated by PE) and plane stress plate specimens (denominated by PS) as sketched in Fig. 3. For RB and PS geometries, tensile tests are performed on both smooth and notched specimens while only notched specimens are considered for the PE geometry.

The specimens undergo different stress states. Given the Cauchy stress tensor $\boldsymbol{\sigma}$ with

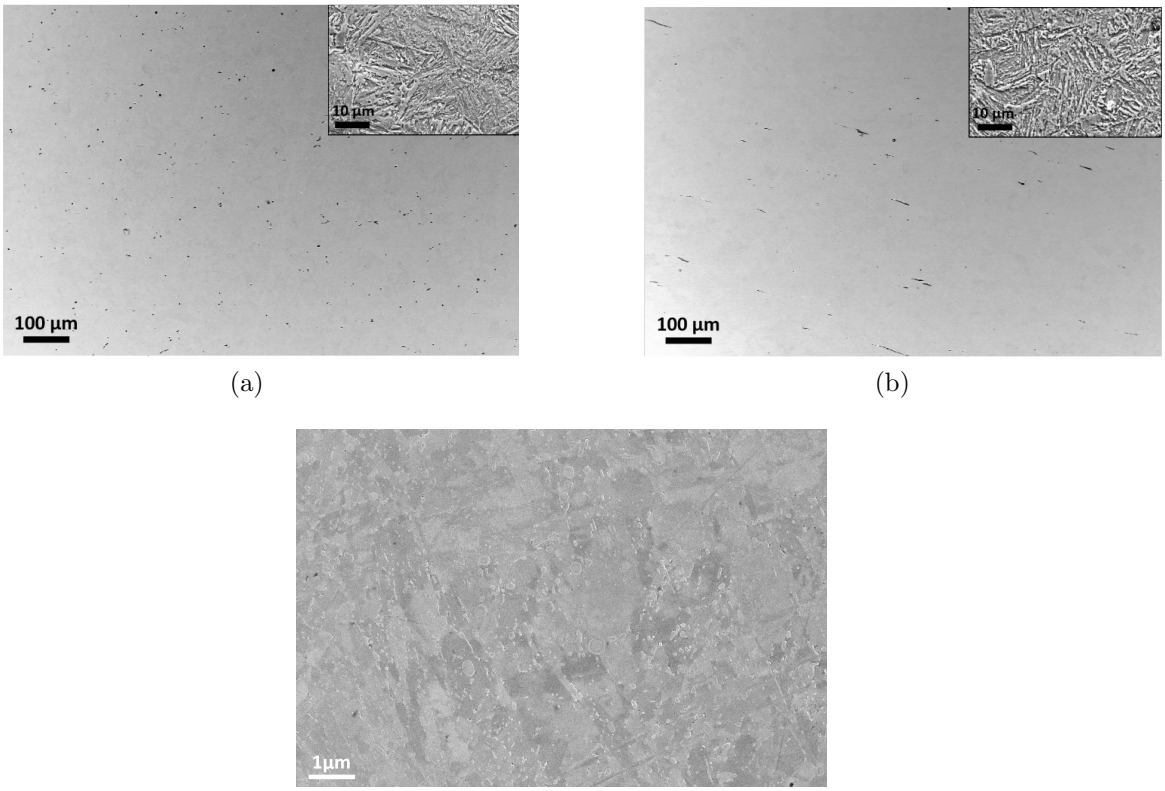

Figure 2: SEM micrographs of the initial microstructure of the investigated HSS: (a) perpendicular to the longitudinal direction, (b) perpendicular to the radial direction, inserts show the martensitic microstructure after etching, and (c) a higher magnification shows the carbides population dispersed in the martensitic matrix.

eigenvalues $\sigma_1 \geq \sigma_2 \geq \sigma_3$, the three invariants can be expressed as

$$\begin{aligned} p' &= \frac{\mathrm{tr}\left(\boldsymbol{\sigma}\right)}{3} = \frac{\sigma_1+\sigma_2+\sigma_3}{3}\,, \\ \sigma_{\mathrm{eq}} &= \sqrt{\frac{3}{2}\mathrm{dev}\left(\boldsymbol{\sigma}\right):\mathrm{dev}\left(\boldsymbol{\sigma}\right)} = \sqrt{\frac{\left(\sigma_1-\sigma_2\right)^2+\left(\sigma_1-\sigma_3\right)^2+\left(\sigma_2-\sigma_3\right)^2}{2}}\,, \text{ and} \\ J_3 &= \det \mathrm{dev}\left(\boldsymbol{\sigma}\right) = \left(\sigma_1-p'\right)\left(\sigma_2-p'\right)\left(\sigma_3-p'\right)\,, \end{aligned} \tag{1}$$

where $\mathrm{tr}\left(\bullet\right)$ and $\mathrm{dev}\left(\bullet\right)$ are respectively the trace and deviatoric operators, and p' and σ_{eq} are known, respectively, as the hydrostatic stress and von Mises equivalent stress. The stress triaxiality (denoted by T) and the Lode parameter[1] (denoted by ζ) are defined as

[1]There exist different ways to define a parameter characterizing the Lode effect [46]: (i) ζ whose definition is given by Eq. (2), (ii) $\theta = \arccos\left(\zeta\right)/3$ which is known as the Lode angle, and (iii) $L = \left(2\sigma_2-\sigma_1-\sigma_3\right)/\left(\sigma_1-\sigma_3\right) = \sqrt{3}\tan\left(\theta-\pi/6\right)$. Without loss of generality, ζ is referred to as the Lode parameter in this work to quantify the Lode effect.

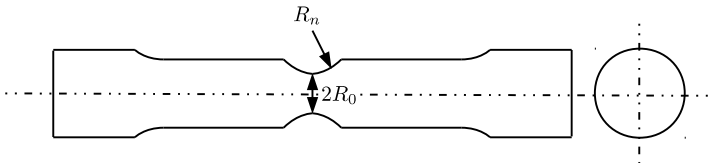

(a) Round bars specimens

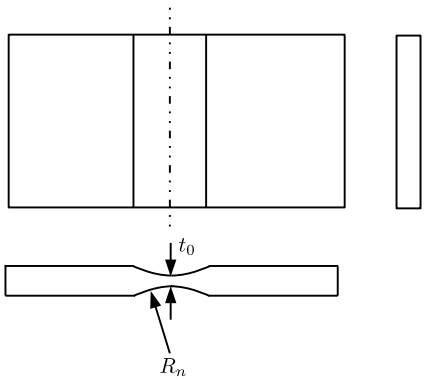

(b) Plane strain specimen,

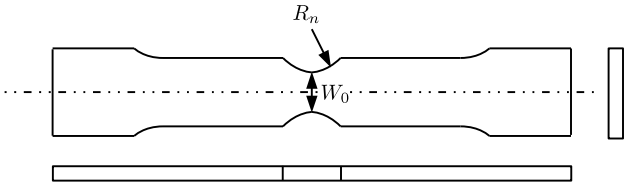

(c) Plane stress specimen

Figure 3: Sample geometries used in this study: (a) round bar (RB) specimens with R_0=3 mm, (b) plane strain (PE) specimens with t_0=2 mm, and (c) plane stress (PS) specimens with W_0=7 mm.

dimensionless quantities from these three stress invariants as

$$T = \frac{p'}{\sigma_{\text{eq}}} \text{ and } \zeta = \frac{27 J_3}{2\sigma_{\text{eq}}^3}\,, \tag{2}$$

with $-\infty < T < +\infty$ and $-1 \leq \zeta \leq 1$. While T quantifies the magnitude of the hydrostatic contribution, ζ indicates the loading mode. It can be shown that $\zeta = 1$ corresponds to an axisymmetric tension, $\zeta = 0$ corresponds to plane strain and general shear loading conditions, and $\zeta = -1$ corresponds to an axisymmetric compression. The pair of dimensionless parameters (T, ζ) is generally used to characterize the stress state.

For RB specimens, the loading conditions at the center of the notched section are $T \geq 1/3$ and $\zeta = 1$. For PE specimens, one has $T \geq 1/\sqrt{3}$ and $\zeta = 0$ as a result of the plane strain condition. The design of the PS specimens is expected to result Lode parameter values in the range [0 1] while the range of stress triaxiality is the same as in the RB and PE specimens.

The presence of the notch (in the RB, PE, and PS specimens shown in Fig. 3) is characterized by the shape factor, denoted by γ and defined as

$$\gamma = \frac{a_0}{R_n}\,, \tag{3}$$

where R_n is the notch radius and a_0 is defined based on the specimen type: (i) for RB specimens, $a_0 = R_0$ where R_0 is the initial radius at the notched section, (ii) for PE specimens, $a_0 = t_0/2$ where t_0 is the initial in-plane thickness at notched section, and (iii) for PS specimens, $a_0 = W_0/2$ where W_0 is the initial width at the notched section. For smooth specimens, $\gamma = 0$ since $R_n \to \infty$. The level of the stress triaxiality at the center of the notched section increases with the shape factor γ [15, 19, 21].

Table 1: Sample names with their key parameters

Type	Test	Direction	γ	T^*	ζ^*
Smooth round bars	SRB	L, T	0	$\geq 1/3$	1
Notched round bars	NRB-1	L, T	0.75	$> 1/3$	1
Notched round bars	NRB-2	L, T	1.5	$> 1/3$	1
Notched round bars	NRB-3	L, T	2	$> 1/3$	1
Notched round bars	NRB-4	L	3	$> 1/3$	1
Notched plane strain	NPE-1	L	0.1	$> 1/\sqrt{3}$	0
Notched plane strain	NPE-2	L	1/3	$> 1/\sqrt{3}$	0
Notched plane strain	NPE-3	L	1	$> 1/\sqrt{3}$	0
Smooth plane stress	SPS	L	0	$\geq 1/3$	[0 1]
Notched plane stress	NPS-1	L	0.75	$> 1/3$	[0 1]
Notched plane stress	NPS-2	L	1.5	$> 1/3$	[0 1]
Notched plane stress	NPS-3	L	2.9	$> 1/3$	[0 1]

* The exact values of the stress triaxiality T and of the Lode parameter ζ at failure at the notched section will be estimated in Section 4.

Different values of the shape factor are considered for each specimen type (including RB, PE, and PS specimens) which allows studying the dependencies of the fracture strain on the stress triaxiality and Lode parameter. The labeling of each specimen is summarized in Table 1. A prefix S is used for the smooth (unnotched) specimens and a prefix N for the notched ones. The RB specimens are extracted in both longitudinal direction (notation prefixed by L) and transverse direction (notation prefixed by T). Since other specimens are extracted only following the longitudinal direction due to geometrical constrains, their prefix L- is omitted for conciseness.

2.3. Damage characterization methods

The porosity distribution, on both the L-SRB and T-SRB specimens loaded up to fracture, is measured along their axisymmetric axis following the approach employed in [47]. The specimens were first cut following their axis, then micrographs of the microstructure were taken with the electronic microscope (SEM) from the failure surface along the complete necking distance, see Fig. 4. From these micrographic images, the density of cavities along the axisymmetric axis can be extracted by observation. Since the plastic deformation, which is large close to the crack surface and decreases when the distance from the crack surface increases, can be quantified in terms of the distance from the crack using a validated numerical simulation, a continuous nucleation law can be identified in function of the plastic deformation, see Section 5.

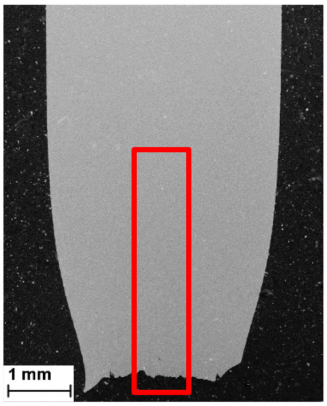

Figure 4: Rectangular region used for the measurement of the porosity after the final failure of the SRB specimen.

3. Experimental results

3.1. Mechanical tests

3.1.1. Tensile tests on RB specimens

For each test performed on RB specimens, see Fig. 3a, several (typically 3 repetitions) specimens were considered to assess the variability in the mechanical response. The specimens were loaded using a displacement control at constant speed equal to 1mm/min. All tests were conducted until final fracture. For the SRB specimens, the extensometer is used to measure the elongation ΔL over a reference gauge length $L_0 = 30$mm, from which the engineering strain is estimated as $\Delta L/L_0$. For the NRB-1, NRB-2, NRB-3, and NRB-4 specimens, a strictometer is used to measure the reduction of radius ΔR at the minimum notched section whose initial radius is R_0. The engineering stress is evaluated by F/S_0 where F is the axial tensile force and $S_0 = \pi R_0^2$ is the initial smallest cross-section area of the specimen[2]. A stress triaxiality $T \geq 1/3$ is expected for these tests while the Lode parameter ζ is equal to 1 at the ligament center.

Figure 5a shows the engineering curves obtained on the L-SRB and T-SRB specimens. Prior to the onset of fracture defined by the point at which the stress value suddenly drops, the two curves are close to one another. This agrees with the observations in Section 2.1 reporting no crystallographic anisotropy between the longitudinal and transverse directions. However, a significant anisotropy on the fracture strain is observed: fracture occurs earlier in the transverse direction. This anisotropy results from the distribution of the elongated MnS inclusions, for which larger voids nucleate and grow faster when the structure is loaded in the transverse direction. A micro-mechanics based explanation of these mechanisms is provided in Section 3.2.

Figure 5b shows typical engineering curves obtained from the tensile tests on the L-NSB specimens. It can be seen that a smaller notch radius (characterized by a larger shape factor

[2]For confidentiality reasons, the experimental results are provided using normalized values of the axial force with respect to a reference value.

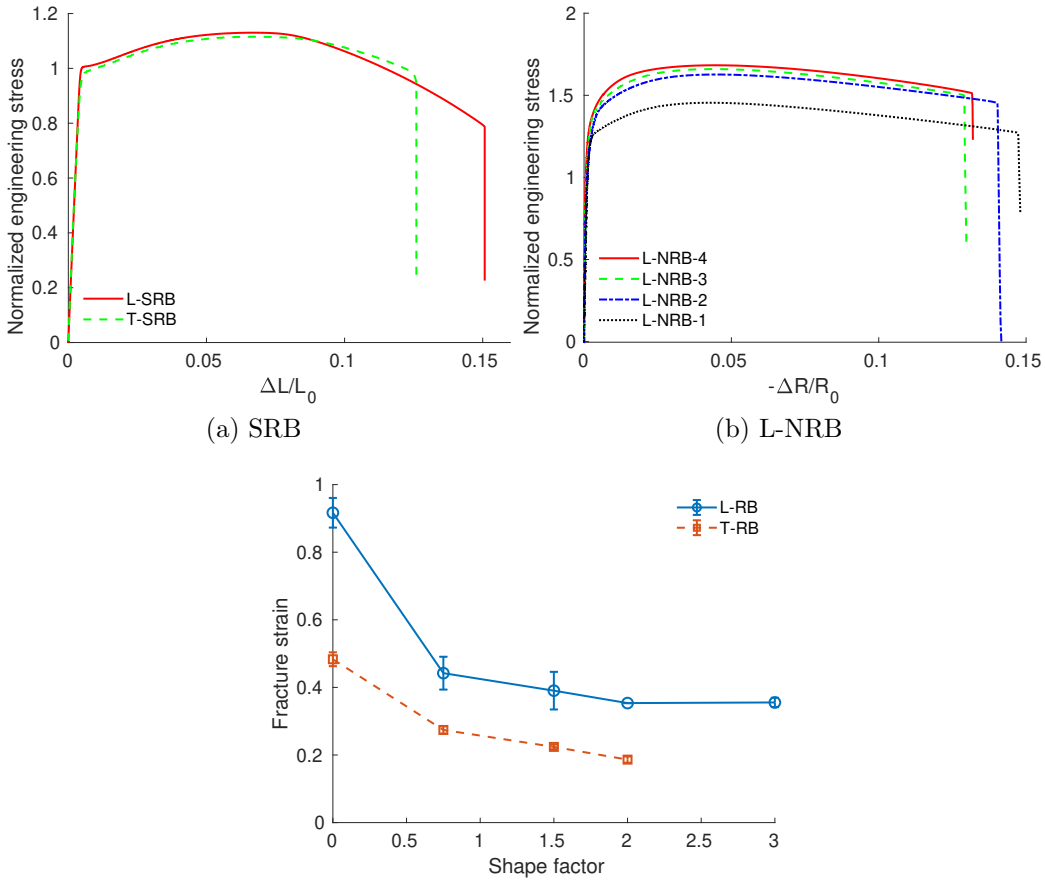

(a) SRB (b) L-NRB

(c) Fracture strain

Figure 5: RB specimens: (a) typical experimental curves of the normalized engineering stress in terms of the relative elongation $\Delta L/L_0$ for the L-SRB and T-SRB specimens, (b) typical experimental curves of the normalized engineering stress in terms of the relative radius reduction $-\Delta R/R_0$ for the L-NRB specimens, and (c) fracture strain in terms of the shape factor. Only a typical curve among the available experimental results of each geometry is shown.

γ) results in an increase of the stress levels and in earlier failure as a result of a higher stress triaxiality.

The fracture strain defined as the mean equivalent plastic strain of the matrix at the onset of failure is widely used to quantify the material ductility. With the axisymmetric (both SRB and NRB) specimens, the fracture strain is estimated from the reduction of the cross-section area [48] as

$$\bar{\epsilon}_{\mathrm{f}} = 2 \ln \frac{R_0}{R_{\mathrm{f}}}, \tag{4}$$

where R_0 is either the initial radius of the SRB specimens or the radius at the notched section of the NRB specimens, and R_{f} is its value at fracture. This $\bar{\epsilon}_{\mathrm{f}}$ is a mean value at the level of the cross-section and not exactly the very local value at the first point of cracking. The value of R_{f} of each specimen is measured after fracture instead of using the strictometer to

get the best accuracy, so that the fracture strain is not estimated directly from Fig. 5b. The dependence of the fracture strain on the shape factor in these tests is shown in Fig. 5c: the fracture strain decreases with increasing stress triaxiality. Furthermore, the fracture strain in the transverse specimens is almost 50 % lower than in the longitudinal ones under the same loading conditions.

Figures 6a-6c show fracture surfaces of the L-SRB and Figs. 6d-6e of the T-SRB specimens. The well-known cup-cone failure profile is clearly visible. In both cases, the fracture surface consists of a flat part with a rough appearance due to the micro-voids at the center and a less rough slant part near the free surface. The slant part, inclined at 45^o compared to the loading direction, corresponds to the zone of failure induced by shear localization and exhibits a different surface aspect. When loaded along the transverse direction, as shown in Fig. 6e, the central part seems fibrous, this pattern being dictated by the prolate MnS inclusions loaded perpendicularly. Smaller voids nucleated around the carbide inclusions are also observed.

The typical cup-cone failure profile is very clear with the L-NRB (-1, -2, and -4) specimens as shown in Figs. 7. Micrometer-sized dimples are the remnants of the voids formed around MnS particles which coalesced together by tensile internal necking during the last steps of the failure process. At the bottom of the dimples, a segment of the inclusion is sometimes still visible (see e.g. Fig. 7e). Smaller nanometric dimples are the results of voids created from carbides decohesion.

The fraction of the flat part of the total fracture surface of the RB specimens is reported in Fig. 8. This fraction depends not only on the shape factor of the specimens but also on the direction from which the specimens are extracted. The dependence on the shape factor is more pronounced for the L-RB specimens than for the T-RB specimens.

3.1.2. Tensile tests on PE specimens

The PE specimens, see Fig. 3b, were loaded under displacement control at constant speed equal to 1mm/min. All the tests were conducted until final fracture. The extensometer is used to measure the elongation ΔL over a reference gauge length $L_0 = 18$mm, from which the engineering strain is estimated as $\Delta L/L_0$. A strictometer is also used to measure the thickness reduction Δt in the notched section. The engineering stress is estimated by F/S_0 where F is the axial tensile force and S_0 is the initial minimum cross-section area of the specimen.

The force evolution is represented in Fig. 9a as a function of the engineering strain. Reducing the notch radius induces a higher apparent elastic stiffness and a higher level of tensile stress due to a higher stress triaxiality in the centre of the specimen.

For this geometry, the equivalent fracture strain can be estimated by [48]

$$\bar{\epsilon}_{\mathrm{f}} = \frac{2}{\sqrt{3}} \ln \frac{t_0}{t_{\mathrm{f}}}\,, \tag{5}$$

where t_0 is the initial in-plane thickness at notched section and t_{f} is the in-plane thickness at fracture. The value of t_{f} of each specimen is measured once final failure occurs. The experimental measurements are gathered in Fig. 9c in terms of the shape factor. As expected, the ductility decreases with decreasing notch radius. However, the fracture strain is smaller compared to the axisymmetric cases with the main axis in the longitudinal direction as reported

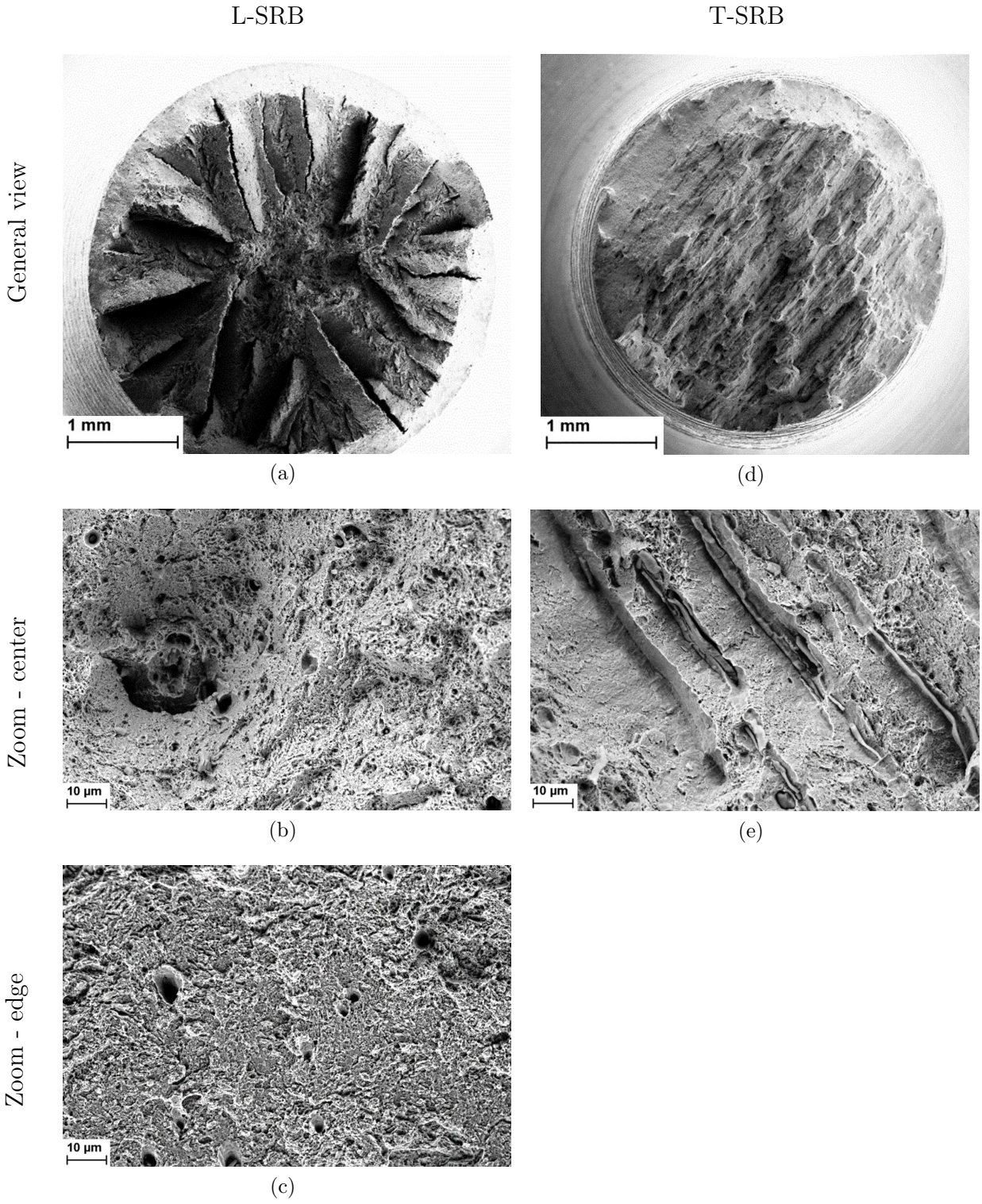

Figure 6: SRB specimens - micrographs of the fracture surface: (a - c) for a L-SRB specimen, and (d, e) for a T-SRB specimen.

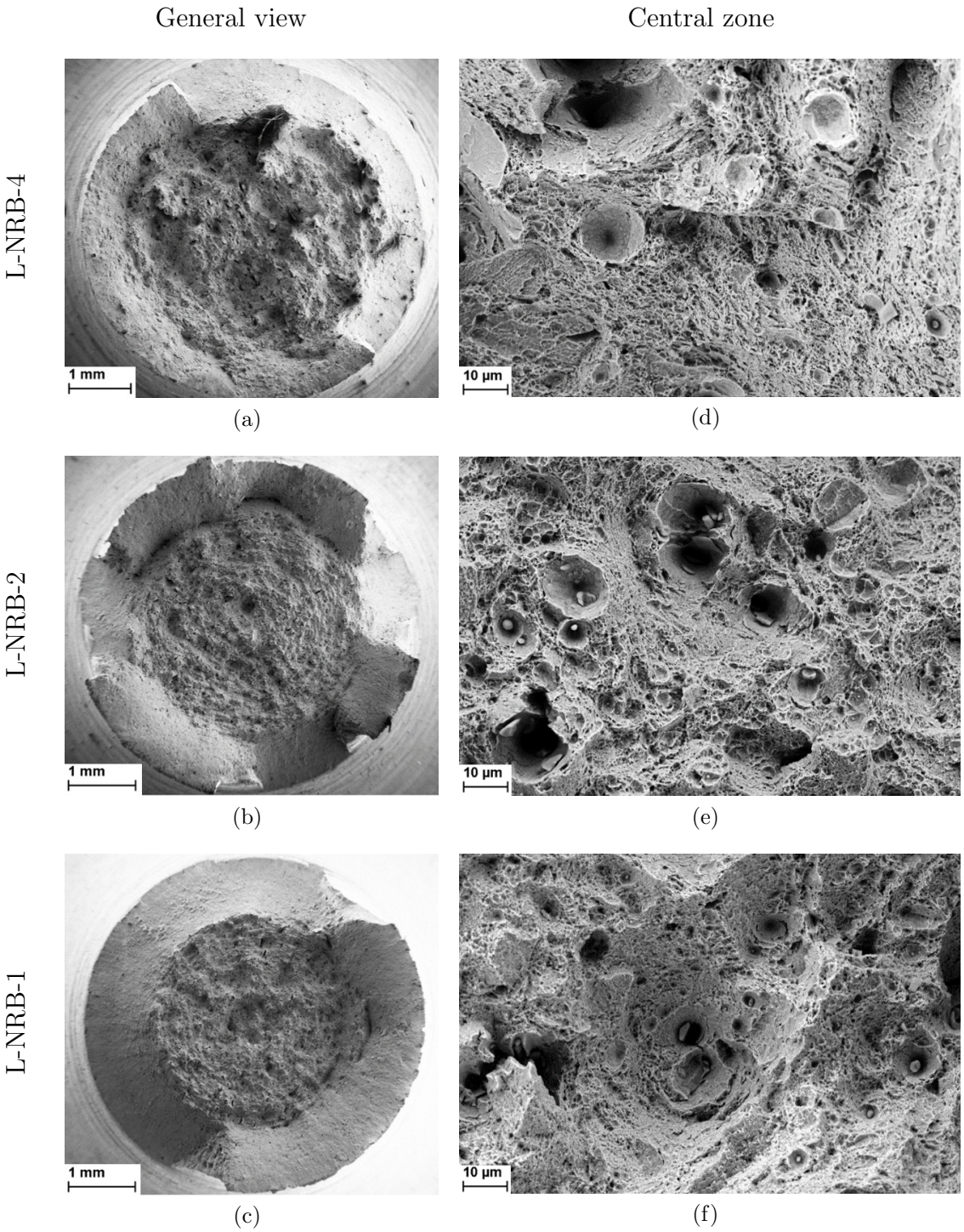

Figure 7: RB specimens - micrographs of the L-NRB specimens: (a-c) fracture surface for the different notch radii, and (d-f) zoom on the central part.

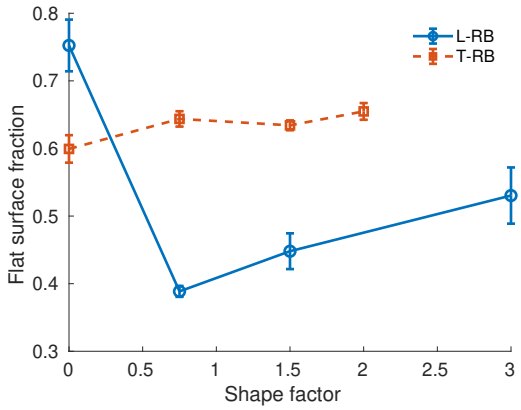

Figure 8: RB specimens: variation of the fraction of the flat part of the fracture surface as a function of the notch shape factor for the two orientations L and T.

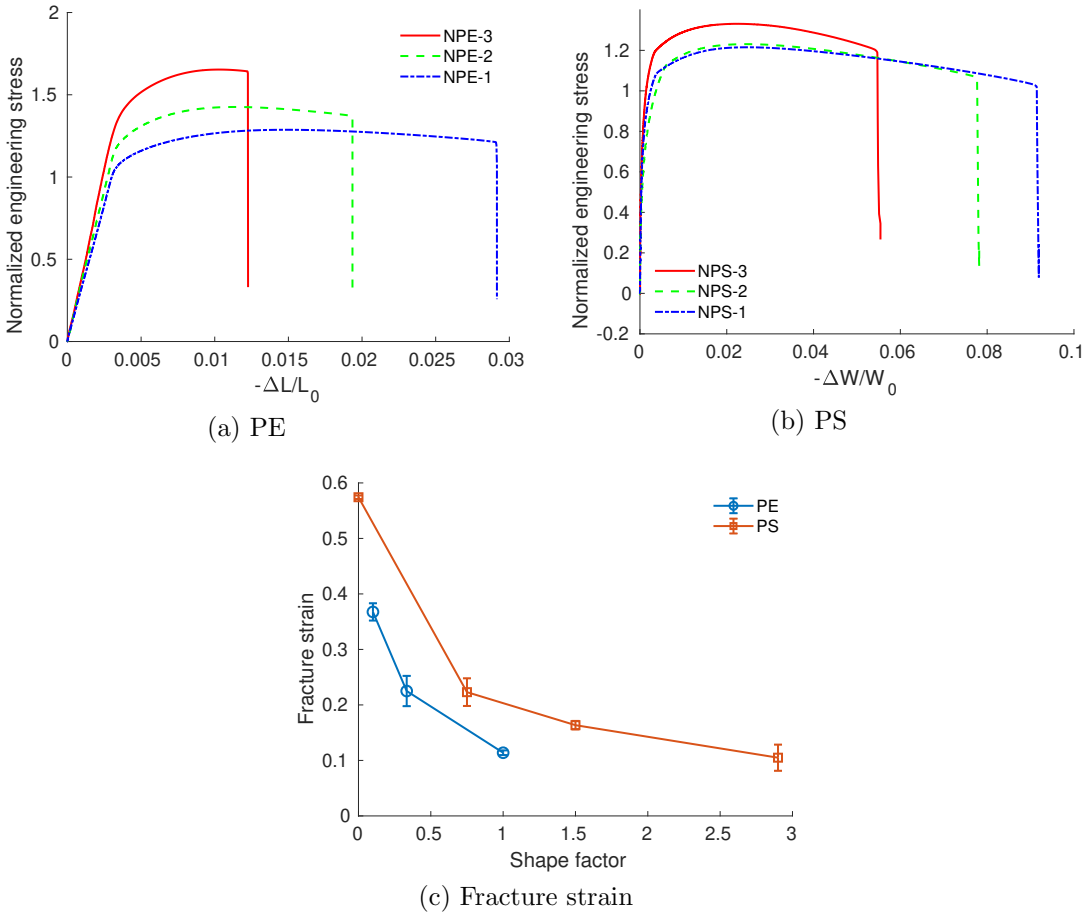

(a) PE

(b) PS

(c) Fracture strain

Figure 9: PE and PS specimens: (a) normalized engineering stress as a function of the engineering strain $\Delta L/L_0$ of the PE specimens, (b) normalized engineering stress versus the engineering strain $\Delta W/W_0$ of the PS specimens, and (c) fracture strain in terms of the notch shape factor. Only one typical curve among the available experimental results of each geometry is shown in (a) and (b).

in Fig. 5c, which can be explained by the additional Lode-induced damage contribution resulting from the plane strain condition.

Figure 10 shows the fracture surfaces corresponding to the PE specimens exhibiting a slant fracture mode for the three groove radii. The fracture surface is characteristic of a macroscopic shear failure mode along the sides with flat voids and an intervoid necking void coalescence process in the center. The latter is more visible on the NPE-3 specimen for which the stress triaxiality is the highest.

3.1.3. Tensile tests on PS specimens

For each test on the PS specimens, see Fig. 3c, several repetitions were considered to assess the material and test variability. The specimens were loaded under a displacement control at constant speed equal to 1mm/min. All the tests were conducted until final fracture of the specimens. A strictometer was used to measure the width reduction ΔW at the notched section whose initial width is W_0. The engineering stress is estimated by F/S_0 where F is the axial tensile force and S_0 is the initial cross-section area.

The evolution of the tensile force in terms of the relative width reduction $\Delta W/W_0$ is shown in Fig. 9b. A reduction of the notch radius results in an increase of the applied tensile stress. The notch size affects both the triaxiality and the Lode parameter whose value is not a constant as in the RB and PE specimens.

Based on the rough assumption that the minimum cross-section at fracture remains rectangular, the fracture strain for this geometry can be approximated by

$$\bar{\epsilon}_{\mathrm{f}} = \frac{2}{\sqrt{3}} \sqrt{\ln^2 \frac{W_0}{W_{\mathrm{f}}} + \ln^2 \frac{t_0}{t_{\mathrm{f}}} + \ln \frac{W_0}{W_{\mathrm{f}}} \ln \frac{t_0}{t_{\mathrm{f}}}}\,, \tag{6}$$

where W_0 and W_{f} are respectively the initial specimen width at the notch level and the width at fracture, and where t_0 and t_{f} are respectively the initial thickness at the notch and the thickness at fracture. The values of W_0, W_{f}, t_0, and t_{f} are directly measured on the test specimens. The obtained results are shown in Fig. 9c. The fracture strain decreases with a decreasing notch radius.

3.2. Damage characterization

Typical micrographs with voids are shown in Figs. 11a-11d and Figs. 11e-11f for respectively an L-SRB specimen and a T-SRB specimen. The damage originates early in the process by particle cracking or matrix/particle decohesion, respectively for the L- and T-specimens. Higher magnification observations below the fracture surface in Fig. 11b highlight the decohesion between matrix and secondary carbides population. However, these events are observed at larger plastic strains and just below the fracture surface only.

As shown in Section 3.1, the fracture strain is highly anisotropic. One source of anisotropy originates from the porosity nucleation triggered by the fracture of the elongated MnS inclusion: when loaded along the main particle axis, the MnS inclusions nucleate by particle cracking, while, when loaded in the perpendicular direction, the porosity arises from the matrix/particle decohesion, as illustrated in Fig. 12. In both cases, void nucleation occurs early in the loading process but the voids nucleate differently depending on the loading direction, a phenomenon known in the literature for a long time [6].

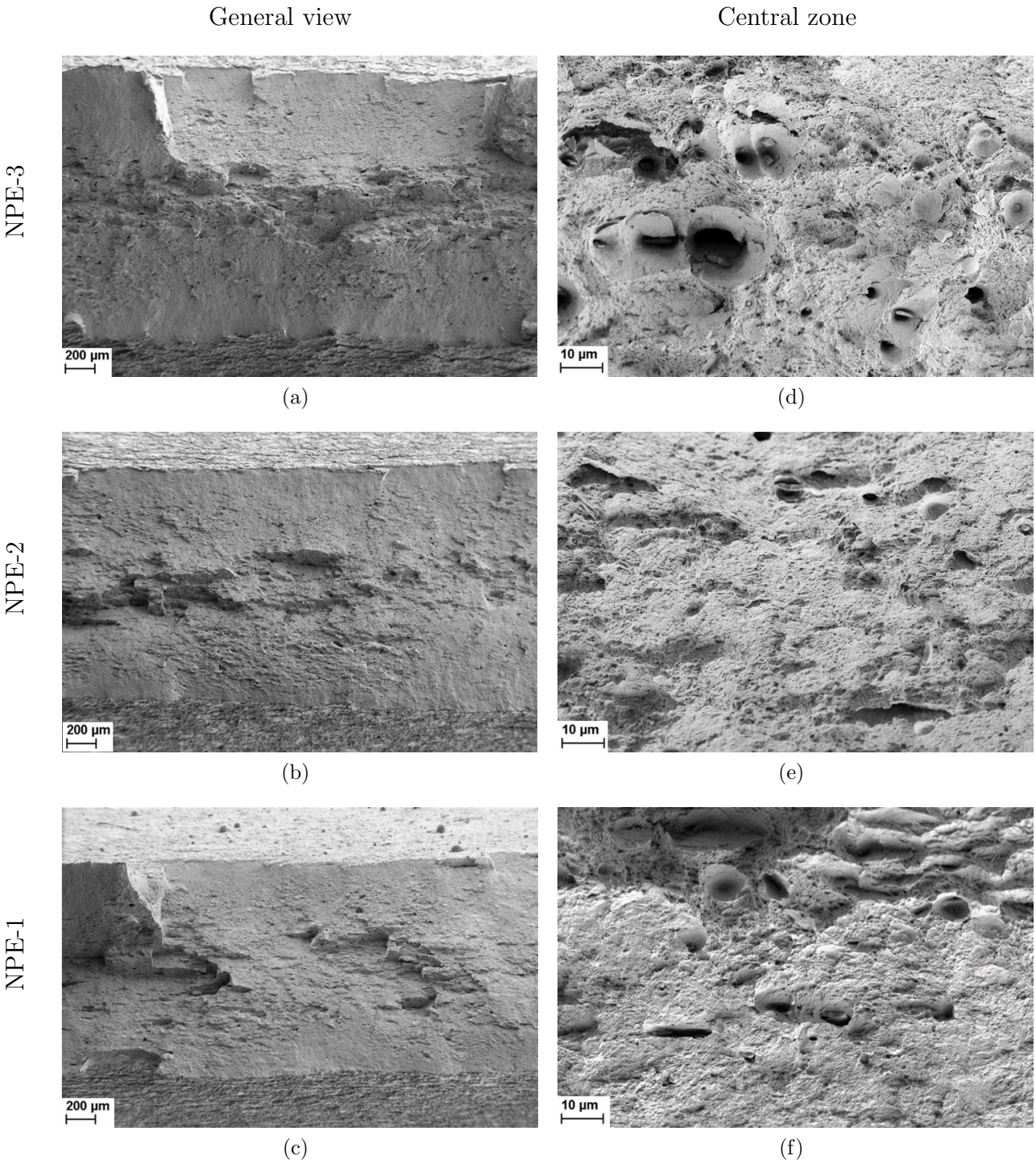

Figure 10: PE specimens - micrographs: (a-c) fracture surface for the different notch radii, and (d-f) zoom on the central part.

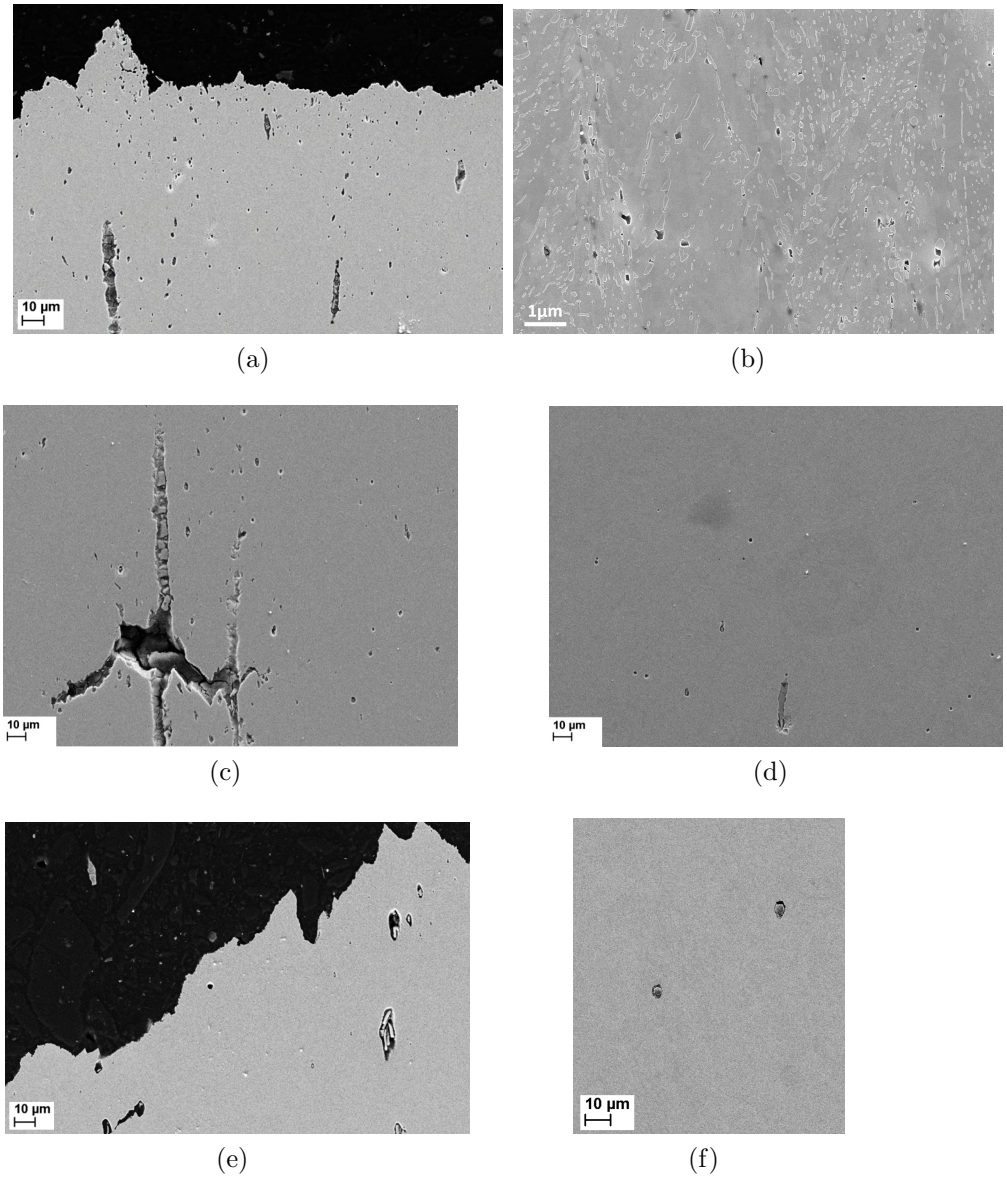

(a) (b)

(c) (d)

(e) (f)

Figure 11: Examples of micrographs obtained at different distances from the crack surface - L-SRB specimen (a-d): (a) just below the fracture surface, (b) high magnification of the damaged microstructure below the fracture surface, (c) example of void coalescence below the crack surface, and (d) at initiation of necking - T-SRB specimen (e, f): (e) just below the crack surface and (f) at the middle of the necking zone.

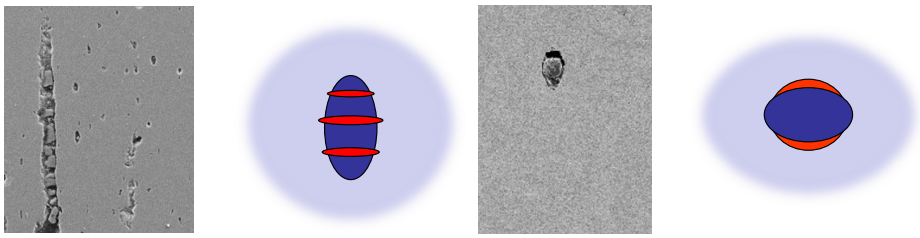

(a) L-specimen (b) T-specimen

Figure 12: Illustration of the porosity nucleation triggered by the fracture of the elongated MnS inclusion, zooms from Fig. 11 and schematic representation: (a) nucleation by particle cracking when loaded along the main particle axis, and (b) nucleation by matrix/particle decohesion when loaded in the transverse direction.

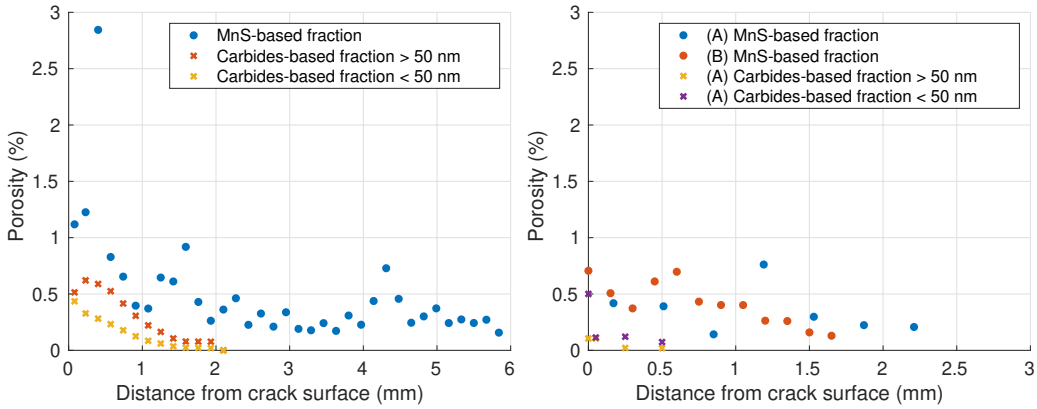

(a) L-SRB (b) T-SRB

Figure 13: Experimental measurements of the different porosity populations (MnS and carbides) in terms of the distance to the fracture surface on: (a) a L-SRB specimen, and (b) two T-SRB specimens (denoted by A and B).

After image processing, the surface fraction of the MnS inclusions and of their associated surrounding cavity is computed. The porosity is then deduced by assuming that the surface fraction is equal to the volumetric fraction, which is the case for random distributed voids. The porosity is then plotted as a function of the distance from the fracture surface in Fig. 13 for both void populations.

4. Elastoplastic behavior

4.1. Hyperelastic-based elastoplastic model

The material model at finite strains is specified as the evolution of the first Piola-Kirchhoff stress tensor (denoted by $\mathbf{P}$) in terms of the deformation gradient (denoted by $\mathbf{F}$) and a set of internal variables (denoted by $\mathbf{Z}$) introduced to capture the history and path dependencies as

$$\mathbf{P} = \mathfrak{P}\left(\mathbf{F}, \mathbf{Z}\right) \ , \text{ and evolution laws for } \mathbf{Z} \, . \tag{7}$$

For elasto-plastic materials, a multiplicative decomposition of the deformation gradient is supposed as

$$\mathbf{F} = \mathbf{F}^{\mathrm{e}} \cdot \mathbf{F}^{\mathrm{p}} \, , \tag{8}$$

where $\mathbf{F}^{\mathrm{e}}$ is its elastic part and $\mathbf{F}^{\mathrm{p}}$ is its plastic part. The elastic behavior is based on a hyperelastic formulation, in which an elastic potential is given by

$$\psi = \frac{K}{2} \left(\ln J^{\mathrm{e}}\right)^2 + \frac{G}{4} \mathrm{dev}\left(\ln \mathbf{C}^{\mathrm{e}}\right) : \mathrm{dev}\left(\ln \mathbf{C}^{\mathrm{e}}\right) \ , \tag{9}$$

where $\mathbf{C}^{\mathrm{e}}$ is the elastic right Cauchy strain tensor, $\mathrm{dev}\left(\mathbf{A}\right)$ represents the deviatoric part of an arbitrary second order tensor $\mathbf{A}$, $J^{\mathrm{e}} = \det \mathbf{F}^{\mathrm{e}} > 0$ is the elastic Jacobian, and K and G are respectively the bulk and shear moduli of the material. The first Piola-Kirchhoff stress tensor $\mathbf{P}$ is estimated from the hyperelastic potential (9) under a purely elastic state (constant $\mathbf{F}^{\mathrm{p}}$) as

$$\mathbf{P} = \frac{\partial \psi}{\partial \mathbf{F}} = K \mathbf{F}^{-T} \ln J^{\mathrm{e}} + \mathbf{F}^{\mathrm{e}} \cdot \left[G \mathbf{C}^{\mathrm{e}-1} \cdot \mathrm{dev}\left(\ln \mathbf{C}^{\mathrm{e}}\right) \right] \cdot \mathbf{F}^{\mathrm{p}-T} \, . \tag{10}$$

In terms of the elastic logarithmic strain measure, defined as $\mathbf{E}^{\mathrm{e}} = \frac{1}{2} \ln \mathbf{C}^{\mathrm{e}}$, Eq. (9) allows defining the logarithmic stress measure $\boldsymbol{\tau}$, which is energetically conjugate to $\mathbf{E}^{\mathrm{e}}$ as

$$\boldsymbol{\tau} = \frac{\partial \psi}{\partial \mathbf{E}^{\mathrm{e}}} = K \mathrm{tr}\left(\mathbf{E}^{\mathrm{e}}\right) \mathbf{I} + 2G \mathrm{dev}\left(\mathbf{E}^{\mathrm{e}}\right) \ , \tag{11}$$

where $\mathrm{tr}\left(\mathbf{A}\right)$ represents the trace of an arbitrary second order tensor $\mathbf{A}$. One can demonstrate that $\boldsymbol{\tau}$ is interpreted as the Kirchhoff stress represented in the elastic corotational space [49]. This stress measure relates to the first Piola-Kirchhoff stress tensor $\mathbf{P}$ as a results of Eqs. (10, 11) by the following relation

$$\boldsymbol{\tau} = \mathbf{F}^{\mathrm{e}T} \cdot \mathbf{P} \cdot \mathbf{F}^{\mathrm{p}T} \, . \tag{12}$$

According to the J_2-elastoplasticity theory, the von Mises stress criterion reads

$$\Phi = \frac{\tau_{\mathrm{eq}}}{\tau_{\mathrm{y}}\left(\varepsilon_{\mathrm{m}}\right)} - 1 \leq 0\,, \tag{13}$$

where Φ is the yield function, $\tau_{\mathrm{eq}} = \sqrt{\frac{3}{2}\mathrm{dev}\left(\boldsymbol{\tau}\right) : \mathrm{dev}\left(\boldsymbol{\tau}\right)}$ is the von Mises equivalent stress, τ_{y} is the yield stress that is function of the equivalent plastic strain ε_{m}. The plastic problem is completed by defining an associative and irrotational plastic flow [50] as

$$\mathbf{D}^{\mathrm{p}} = \dot{\mathbf{F}}^{\mathrm{p}} \cdot \mathbf{F}^{\mathrm{p}-1} = \dot{\Lambda}\frac{\partial \Phi}{\partial \boldsymbol{\tau}}\,, \tag{14}$$

where $\mathbf{D}^{\mathrm{p}}$ is the plastic strain rate, and Λ is the plastic multiplier. The evolution of the equivalent plastic strain ε_{m} is given by

$$\dot{\varepsilon}_{\mathrm{m}} = \sqrt{\frac{2}{3}\mathbf{D}^{\mathrm{p}} : \mathbf{D}^{\mathrm{p}}}\,. \tag{15}$$

The numerical integration of the plastic problem follows a predictor-corrector scheme as described in [51]. The parameters of the elastoplastic model consist of the elastic parameters K and G in Eq. (9) and of the hardening law parameters specifying the relation $\tau_{\mathrm{y}}\left(\varepsilon_{\mathrm{m}}\right)$ in Eq. (13).

4.2. Identification of elastoplastic parameters

Prior to necking, the hardening law specifying the function $\tau_{\mathrm{y}}\left(\varepsilon_{\mathrm{m}}\right)$ can be directly identified from the experimental stress-strain curves (see Fig. 5a) using a linear function followed by a power law. During necking, an identification method requiring several iterations has been followed with the goal to match the engineering stress-strain curves obtained by the finite element simulation and by the experimental tests. The hardening law is chosen as

$$\tau_{\mathrm{y}}\left(\varepsilon_{\mathrm{m}}\right) = \begin{cases} \tau_{\mathrm{y}}^0 + h\varepsilon_{\mathrm{m}} & \text{if } \varepsilon_{\mathrm{m}} \leq p_1 \\ \tau_{\mathrm{y1}}\left(\dfrac{\varepsilon_{\mathrm{m}}}{p_1}\right)^{n_1} & \text{if } p_1 < \varepsilon_{\mathrm{m}} \leq p_2 \\ \tau_{\mathrm{y2}}\left(\dfrac{\varepsilon_{\mathrm{m}}}{p_2}\right)^{n_2} & \text{if } \varepsilon_{\mathrm{m}} > p_2 \end{cases}\,, \tag{16}$$

where h, p_1, p_2, n_1, and n_2 are the material parameters, and where $\tau_{\mathrm{y1}} = \tau_{\mathrm{y}}^0 + hp_1$ and $\tau_{\mathrm{y2}} = \tau_{\mathrm{y1}}\left(\frac{p_2}{p_1}\right)^{n_1}$. The values of τ_{y}^0, h, p_1, and n_1 can be directly derived from the experimental data prior to necking, since the plastic state within the gauge length is uniform, while the values of p_2 and n_2 are obtained by curve fitting the engineering stress-strain response obtained by the finite element simulation during necking to the experimental curve.

The finite element meshes used in the elastoplastic simulations are shown in Fig. 14. The RB specimens are modeled with axisymmetric finite elements using 6-node triangular elements. Only the central part of the full specimens is represented, see *e.g.* Figs. 14a and 14b for the cases of SRB and NRB-4 specimens. Plane strain 6-node triangular elements

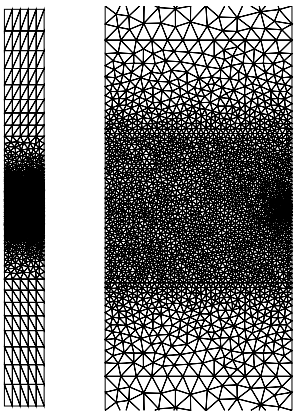

(a) SRB (left) and
zoom at the center (right)

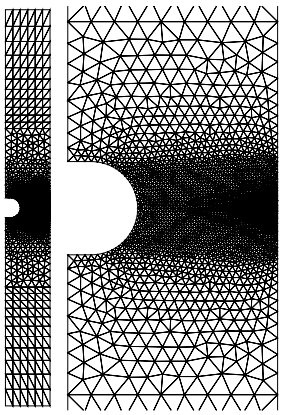

(b) NRB-4 (left) and
zoom at the center (right)

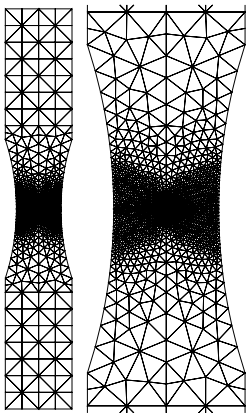

(c) NPE-1 (left) and
zoom at the center (right)

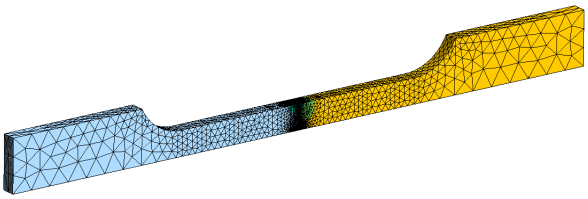

(d) SPS

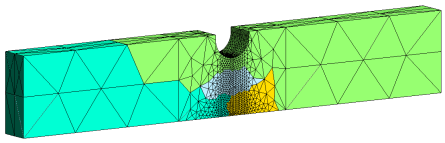

(e) NPS-3

Figure 14: Finite element meshes considered in the elastoplastic simulations: (a) SRB specimen, (b) NRB-4 specimen, (c) NPE-1 specimen, (d) SPS specimen, and (e) NSP-3 specimen.

Table 2: Material properties for the J_2 elastoplastic law.

K [GPa], G [GPa]	Elastic moduli (see Eq. (9))
τ_y^0 [MPa]	Initial yield stress
p_1 [-], n_1 [-], p_2 [-], n_2 [-]	Hardening law parameters (see Eq. (16))

are used to model the tests on PE specimens, see *e.g.* Fig. 14c for the NPE-1 specimen. Besides, because of tolerance issue during the tooling process, the thickness outside of the grooves has been corrected to fit the elastic slope of the experimental tests. The PS specimens need 3-dimensional finite element simulations in which the 10-node tetra elements are used, see *e.g.* Figs. 14d and 14e for the cases of SPS and NPS-3 specimens, in which only half of specimen is meshed because of the geometry and the loading symmetries. All the meshes are refined within the necking or notched regions in order to capture the large local stress and strain gradients. Mesh size sensitivity analyses were systematically performed to ensure a sufficient refinement to produce converged results within the studied range. The symmetry/axisymmetry of the geometry, load, and boundary conditions selected in reduced finite element models affect the prediction of the post-coalescence response and material separation. Indeed, the fracture pattern will be accordingly constrained with these symmetric/axisymmetric assumptions. However, for the RB specimens, the micro-graphs in Figs. 6 and 7 show that the failure surfaces can be qualitatively considered as axisymmetric, which motivates the use of the axisymmetric finite element model. For the PE specimens, the slant failure patterns shown in Fig. 10 require considering a plane strain finite element discretization of the full in-plane thickness of the specimen. For the PS specimens, only a symmetric assumption on the width is considered, and the resulting three-dimensional finite element model can capture the necking phase and can qualitatively reproduce the crack pattern since the latter is normal to the loading direction at the specimens center before exhibiting shear lips at the surface for the smooth ones. Despite of these simplifications, the reduced finite element models drastically decrease the computation time and resources while providing accurate results prior to the onset of fracture.

An average response evaluated from the experimental results on the L-SRB specimens depicted in Fig. 5a is used to conduct the identification of the elastoplastic parameters summarized in Tab. 2. Figure 15a shows, in terms of the stress-strain response, the comparison between the average experimental response obtained for the L-SRB specimens with the numerical simulation after identification. The average result corresponding to the T-SRB specimen is also reported, showing a good agreement and confirming the absence of plastic anisotropy.

In order to further validate the identified parameters of the elastoplastic material model, the other specimen geometries tested experimentally in Section 2 are also simulated. For the different NRB specimen geometries, the average engineering stress-strain curves generated from several test specimens of the same geometry is compared to the numerical predictions in Fig. 15b, showing a good agreement. Figures 15c and 15d respectively compare the specimen simulations to their corresponding average experimental responses. On the one hand, the PS specimens show less sensitivity to the notch radius than the RB and PE specimens. On the other hand, the elastoplastic responses predictions of the PE and PS specimens, respectively reported in Figs. 15c and 15d, are less accurate than the predictions for the NRB specimens

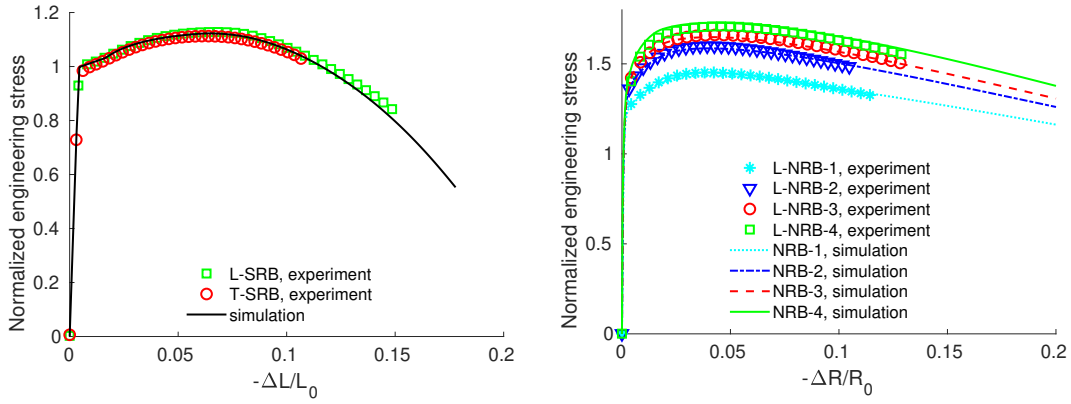

(a) SRB (b) NRB

(c) PE (d) PS

Figure 15: Comparison of the numerical (elastoplastic model) and experimental stress-strain responses: (a) SRB specimens, (b) NRB specimens, (c) PE specimens, and (d) PS specimens. The experimental curves correspond to average responses obtained for different specimens with the same geometry and are truncated once one of the specimen responses exhibits a sudden drop.

shown in Fig. 15b. This can be explained by the Lode effect: the Lode parameter is different for the different types of specimen while the elastoplastic constitutive law was calibrated using only the SRB specimen, and thus considering a unique value of the Lode parameter. A better agreement for the PE and PS specimens could have been obtained by considering a plasticity model that includes a Lode effect [18].

4.3. Determination of local stress state in the crack initiation region

Figures 16a, 16b, and 16c show the evolution of the stress triaxiality in terms of the equivalent plastic strain extracted from the finite element solution at the center of the minimum section of all specimens. The experimental fracture point for all the tests is also indicated based on the equivalent fracture strain at the onset of fracture. The stress triaxiality is not constant during the loading but generally increases with plastic deformation. The presence of a notch results in a strong change of the stress triaxiality at the initial stage of plastic deformation followed by a more gradual change. On the contrary, the results on the smooth specimens show a steady increase. Furthermore, modifying the notch radius in the PS specimens results in smaller variation of the stress triaxiality value than for the two others configurations. Hence, the range of stress triaxiality covered by the RB and PE specimens is similar and is wider than in the case of the PS specimens.

Figure 16d shows the evolution of the Lode parameter in terms of the equivalent plastic strain at the center of the notched section for the PS specimens only. The RB and PE specimens are not shown as the Lode parameter is constant and equal to 1 for the former and 0 for the latter. As shown in Fig. 16d, in each PS test, the Lode parameter is not constant but globally decreases with plastic deformation. This impact is more pronounced when the notch radius decreases. A higher notch radius (*i.e.* a smaller shape factor γ) leads to a higher value of the Lode parameter for the same value of the equivalent plastic strain. Moreover, the presence of a notch results in a strong change of the Lode parameter at the initial stage of plastic deformation followed by a more gradual evolution, contrarily to the SPS specimen.

4.4. Influence of the stress state on the fracture strain

Figures 17a and 17b gather the variation of the fracture strain as a function of (a) the stress triaxiality, and (b) the Lode parameter. For the RB and PE specimens with a constant Lode parameter, the fracture strain generally decreases when the stress triaxiality increases, see Fig. 17a. Although the range of stress triaxiality in the RB and PE specimens is similar, the Lode parameter is significantly different leading to different fracture strains. For the PS specimens, both the stress triaxiality and the Lode parameter vary with the notch radius. The fracture strain increases as the Lode parameter increases, see Fig. 17b, while the stress triaxiality does not vary monotonically, see Fig. 17a.

The fracture strains estimated from the experimental tests following Eqs. (4, 5, 6), and used to extract Figs. 17a and 17b are based on the area reduction at the notched section after full fracture. This is the usual experimental definition of the true fracture strain. They however do not correspond to the true local values of the equivalent plastic strain at the onset of failure. The differences between the overall equivalent plastic strain at fracture (averaged over the minimum cross-section) and the local equivalent plastic strain at cracking initiation extracted from the finite element simulations can be analyzed in Fig.

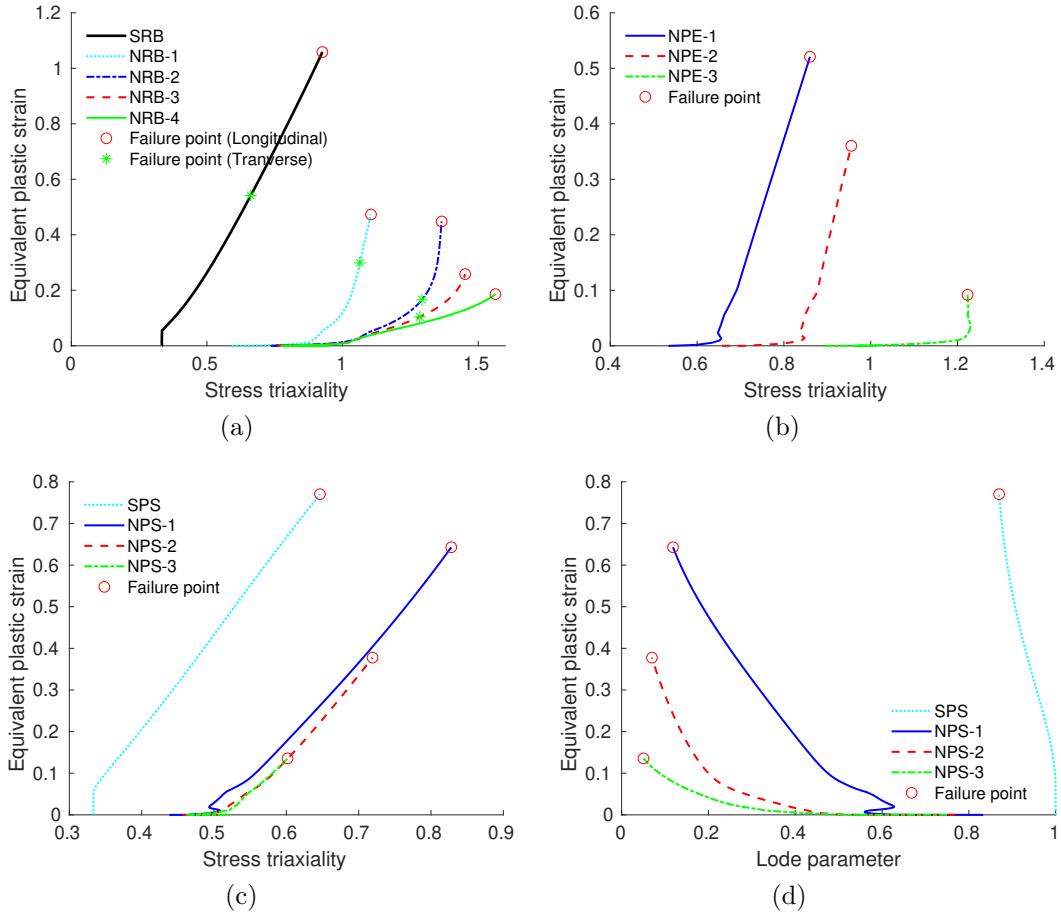

Figure 16: Variation of the predicted (elastoplastic model) stress triaxiality as a function of the equivalent plastic strain at the center of the notched section: (a) RB specimens, (b) PE specimens, and (c, d) PS specimens.

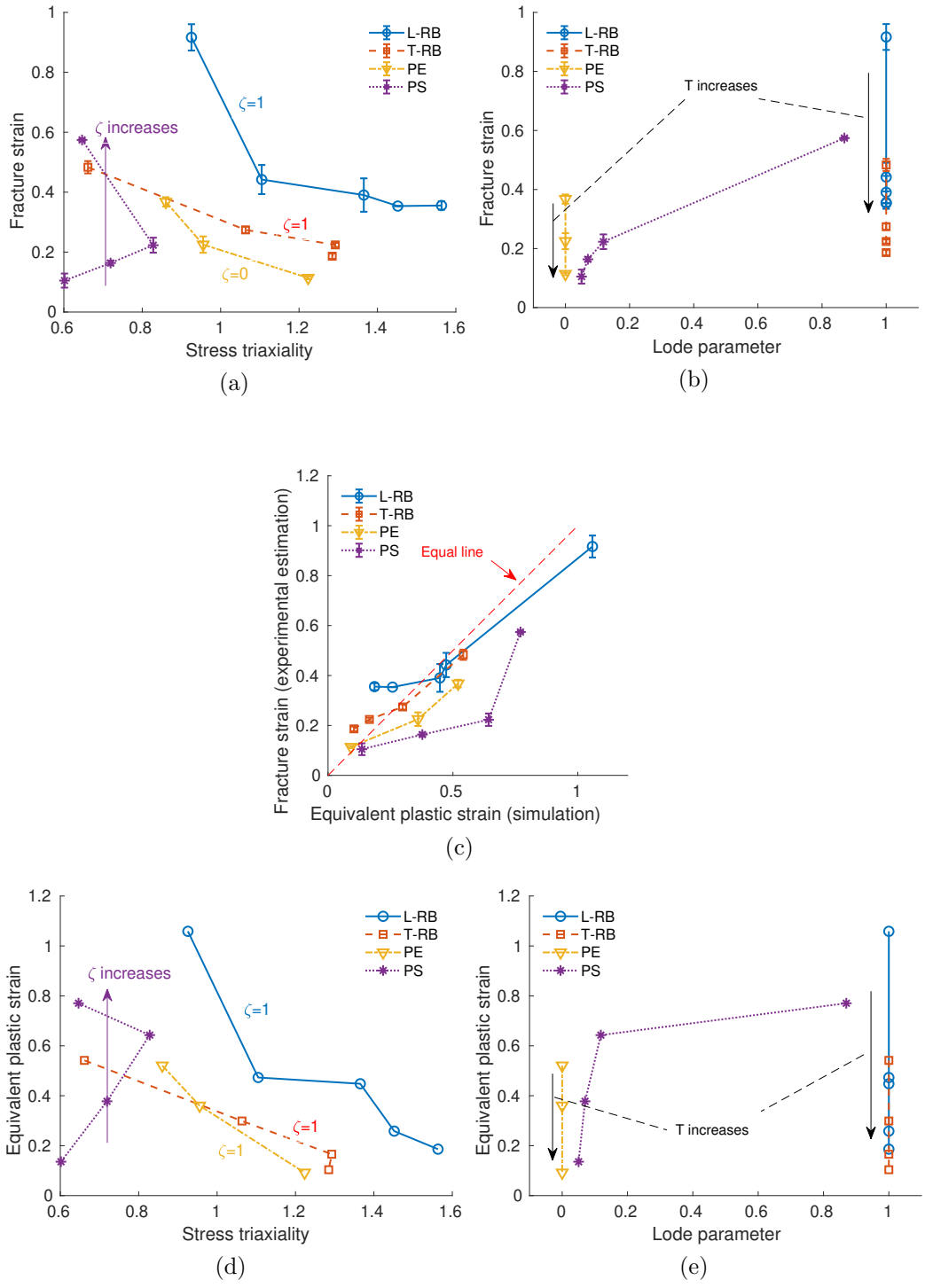

Figure 17: Influence of the stress state on the cracking initiation: (a, b) "experimental" fracture strain, (c) fracture strain estimated by Eqs. (4, 5, 6) from the experimental measurements versus the equivalent plastic deformation extracted from the finite element simulations (elastoplastic model) at the onset of fracture, and (d, e) equivalent plastic strain extracted at the onset of fracture at the necking section.

17c. These differences are due to the fact that, on the one hand, the real distribution of the plastic strain is not uniform, and on the other hand, the failure surface is not perfectly flat leading to uncertainties in the determination of a true fracture area. Moreover, the inaccurate predictions of the fracture strain for the PS specimens result from the assumption that the failure surface remains rectangular. The failure locus depicted in Figs. 17a and 17b in terms of the fracture strain can be reevaluated in terms of the local equivalent plastic strain, see Figs. 17d and 17e with no change in the trend.

The experimental fracture strains defined by Eqs. (4, 5, 6) are all macroscopic quantities. Although these macroscopic values are approximations of the stress and strain states of the location and instant of cracking initiation in the minimum cross-section, they still provide reasonable trends in terms of the impact of the stress triaxiality and of the Lode parameter as shown in Figs. 17a and 17b.

5. Anisotropic void nucleation model and parameters identification

This section is devoted to an extension of the Beremin nucleation model [12] in the context of the Gurson- Tvergaard- Needleman (GTN) model [25, 26, 27]. The goal is to introduce the morphological anisotropy effect in the GTN model through a proper formulation of the void nucleation model. The parameters of the nucleation law are identified and validated based on the damage and microstructure characterization.

5.1. GTN model

In the GTN model [25, 26, 27], the behavior of the matrix obeys the J_2 plasticity model described in Section 4.1. The yield function of the GTN model takes the following form

$$\Phi_{\mathrm{g}} = \left(\frac{\tau_{\mathrm{eq}}}{\tau_{\mathrm{y}}}\right)^2 + 2 f_V q_1 \cosh\left(\frac{3}{2} q_2 \frac{p}{\tau_{\mathrm{y}}}\right) - q_1^2 {f_V}^2 - 1\,, \tag{17}$$

in which $\tau_{\mathrm{eq}} = \sqrt{\frac{3}{2}\mathrm{dev}\left(\boldsymbol{\tau}\right) : \mathrm{dev}\left(\boldsymbol{\tau}\right)}$ is the von Mises equivalent stress, $p = \frac{\mathrm{tr}(\boldsymbol{\tau})}{3}$, f_V is the porosity, and q_1 and q_2 are two material constants, which were introduced to improve the model prediction.

Similar to Eq. (14), the associative plastic flow rule reads

$$\mathbf{D}^{\mathrm{p}} = \dot{\mathbf{F}}^{\mathrm{p}} \cdot \mathbf{F}^{\mathrm{p}-1} = \dot{\Lambda} \frac{\partial \Phi_{\mathrm{g}}}{\partial \boldsymbol{\tau}}\,, \tag{18}$$

where $\dot{\Lambda}$ is the plastic multiplier and $\frac{\partial \Phi_{\mathrm{g}}}{\partial \boldsymbol{\tau}}$ is the normal to the yield surface Φ_{g}.

The evolution of the porosity f_V results from different contributions as

$$\dot{f}_V = \underbrace{\left(1 - f_V\right) \mathrm{tr}\left(\mathbf{D}^{\mathrm{p}}\right)}_{\dot{f}_{V\,\mathrm{gr}}} + \dot{f}_{V\,\mathrm{nu}} + \underbrace{k_\omega \left(1 - \zeta^2\right) f_V \frac{\mathrm{dev}\left(\boldsymbol{\tau}\right) : \mathbf{D}^{\mathrm{p}}}{\tau_{\mathrm{eq}}}}_{\dot{f}_{V\,\mathrm{sh}}}\,, \tag{19}$$

where the first term $\dot{f}_{V\,\mathrm{gr}}$ (so-called growth term) is the usual term associated to the plastic incompressibility of the matrix [26, 27]; the second term $\dot{f}_{V\,\mathrm{nu}}$ (so-called nucleation term) is the contribution of new voids nucleated due to particle debonding or cracking [9]; and the

third term $\dot{f}_{V\mathrm{sh}}$ (so-called shear term) is not present in the original GTN model but was proposed by Nahshon and Hutchinson [16] based on heuristic arguments to account for void deformation and reorientation occurring under low stress triaxiality and shear-dominated distortions. In the shear term, k_ω is a material constant and ζ is the Lode parameter defined in Eq. (2). In the following, since the void growth term $\dot{f}_{V\mathrm{gr}}$ and the heuristic Nahshon-Hutchinson shear term $\dot{f}_{V\mathrm{sh}}$ in Eq. (19) do not incorporate the effects of the void shape, the failure anisotropy observed in Section 3.1 is captured only through the anisotropic micromechanics based nucleation law governing the term $\dot{f}_{V\mathrm{nu}}$. In this nucleation law, the void nucleation intensity changes with the prescribed loading direction through an activation condition based on the Beremin model [12]. Nevertheless, considering the shear-enhanced void growth term $\dot{f}_{V\mathrm{sh}}$ remains necessary, not only under shear dominated conditions, but also to introduce a correction on the void evolution since the GTN model considers the growth of spherical voids, which are only effective representations of the true voids. Indeed, the voids tend to elongate and rotate under significant Lode effect, leading to major changes of void shape. One should distinguish between failure at combined shear and tension loading (corresponding to $\zeta = 1$) versus shear and compression (corresponding to $\zeta = -1$) as revealed by recent micromechanics based cell-model studies [46]. However, since this work investigates the failure under combined shear and tension only, the Nahshon-Hutchinson shear extension is considered, in particular in Part II. In the subsequent analyses, this enhanced term can be neglected as only the failure of the SRB specimens is considered.

The evolution law for the isotropic yield stress τ_{y} is expressed through the mean equivalent plastic strain of the matrix ε_{m} through the hardening law. The evolution law for ε_{m} is then determined under the assumption that the rate of current plastic work is equal to the rate of plastic work in the matrix [25, 26, 27]

$$\boldsymbol{\tau} : \mathbf{D}^{\mathrm{p}} = (1 - f_{V0})\, \tau_{\mathrm{y}} \dot{\varepsilon}_{\mathrm{m}} \,, \tag{20}$$

where $\boldsymbol{\tau} : \mathbf{D}^{\mathrm{p}}$ characterizes the total plastic dissipation and f_{V0} is the initial porosity.

The numerical integration of the plastic problem as well as the finite element framework are detailed in [52]. Hereafter, we formulate the void nucleation contribution $\dot{f}_{V\mathrm{nu}}$ in Eq. (19) in order to account for the anisotropy effects.

5.2. Anisotropic nucleation model

We assume that the anisotropy results only from the porosity nucleation step triggered by the fracture of the elongated MnS inclusion as illustrated in Fig. 12 and discussed in Section 3.2. This anisotropic effect is accounted for by considering an effective micromechanics-based nucleation law based on the original model of the Beremin group of scientists [12].

5.2.1. Strain-based nucleation model with an activation condition

The starting point is to rewrite the nucleation term $\dot{f}_{V\mathrm{nu}}$ in Eq. (19) as

$$\dot{f}_{V\mathrm{nu}} = \begin{cases} A_{\mathrm{n}} \dot{\varepsilon}_{\mathrm{m}} & \text{once } \Phi_{\mathrm{n}} \geq 0 \text{ has been met during the loading history}\,, \\ 0 & \text{otherwise}\,, \end{cases} \tag{21}$$

in which A_n is the parameter controlling the void nucleation intensity, depending not only on the mean equivalent plastic strain of the matrix ε_{m} but also on the loading direction, and

Φ_n is the void nucleation activation function expressed in the next section. Following Eq. (21), the voids nucleate for any subsequent stress level that yields plastic deformation once the condition $\Phi_{\mathrm{n}} \geq 0$ has been met during the loading history. Additionally, one can define p_{c}, which is the value of ε_{m} at the onset of void nucleation, *i.e.* the value of ε_{m} when $\Phi_{\mathrm{n}} \geq 0$ is first satisfied. The void nucleation intensity A_{n} is expressed as a function of the direction $\mathbf{n}^*$ obeying a Gaussian distribution in the spirit of the Chu and Needleman pioneering model [9]

$$A_{\mathrm{n}}\left(\varepsilon_{\mathrm{m}}, \mathbf{n}^*\right) = \frac{\mathbf{n}^* \cdot \mathbf{f}_{\mathrm{n}} \cdot \mathbf{n}^*}{s_{\mathrm{N}}\sqrt{2\pi}} \exp\left[-\frac{1}{2}\left(\frac{\varepsilon_{\mathrm{m}} - p_{\mathrm{c}} - p_{\mathrm{N}}}{s_{\mathrm{N}}}\right)^2\right], \tag{22}$$

where s_{N} and p_{N} are the material constants and $\mathbf{f}_{\mathrm{n}}$ is a tensorial quantity, from which $\mathbf{n}^* \cdot \mathbf{f}_{\mathrm{n}} \cdot \mathbf{n}^*$ defines the fraction of voids nucleated per unit volume following the direction $\mathbf{n}^*$. Only ellipsoidal inclusions are considered in this work. For an ellipsoidal inclusion of longitudinal axis $\mathbf{n}_{\mathrm{long}}$, $\mathbf{f}_{\mathrm{n}}$ takes the form

$$\mathbf{f}_{\mathrm{n}} = f_{\mathrm{nL}} \mathbf{n}_{\mathrm{long}} \otimes \mathbf{n}_{\mathrm{long}} + f_{\mathrm{nT}} \left(\mathbf{I} - \mathbf{n}_{\mathrm{long}} \otimes \mathbf{n}_{\mathrm{long}}\right), \tag{23}$$

where f_{nL} and f_{nT} are two material constants specifying the amount of voids nucleated per unit volume, respectively for uniaxial loading along the longitudinal and transverse directions.

5.2.2. Anisotropic activation condition

The activation condition Φ_{n} in Eq. (21) is developed by borrowing and extending the formulation of the Beremin model [12]. In its original form, void nucleation is activated either by particle cracking or by interface decohesion when the maximum tensile stress in a given particle, σ_{n}, reaches a critical value, σ_{c}, as follows

$$\Phi_{\mathrm{n}} = \sigma_{\mathrm{n}} - \sigma_{\mathrm{c}} \geq 0\,. \tag{24}$$

The value of σ_{n} in Eq. (24) relates to the applied macroscopic stress $\boldsymbol{\tau}$ as

$$\sigma_{\mathrm{n}} = \tau_{\mathrm{I}} + M(\tau_{\mathrm{eq}} - \tau_{\mathrm{y}}^0)\,, \tag{25}$$

where τ_{I} is the largest eigenvalue or the maximum principal stress of $\boldsymbol{\tau}$, τ_{eq} is the macroscopic von Mises stress, τ_{y}^0 is the initial yield stress, and M is a function of the inclusion shape. The advantages of the condition (24) are the possibility to include a stress triaxiality dependency and to take the inclusion shape into account. However, no anisotropy was directly considered in the model.

In this work, the condition (24) is extended by considering the quantities to be directional: M and σ_{c} are no longer represented by scalars but are substituted by second order tensorial quantities $\mathbf{M}$ and $\boldsymbol{\sigma}_{\mathrm{c}}$. The condition (24) is reformulated as finding the direction which maximizes the criterion, i.e

$$\Phi_{\mathrm{n}} = \max_{\mathbf{n}} \left[\mathbf{n} \cdot \boldsymbol{\kappa} \cdot \mathbf{n} + \mathbf{n} \cdot \mathbf{M} \cdot \mathbf{n}(\tau_{\mathrm{eq}} - \tau_{\mathrm{y}}^0) - \mathbf{n} \cdot \boldsymbol{\sigma}_{\mathrm{c}} \cdot \mathbf{n}\right] \geq 0\,, \tag{26}$$

where $\mathbf{n}$ denotes an arbitrary unit vector and $\boldsymbol{\kappa} = \mathbf{P} \cdot \mathbf{F}^T$ is the Kirchhoff stress. Note that $\boldsymbol{\kappa}$ and $\boldsymbol{\tau}$ have the same invariants, as the latter corresponds to the former interpreted in the

elastic corotational space [49]. Clearly, the condition (26) is fulfilled at the eigenvector $\mathbf{n}^*$ associated with the largest eigenvalue of $\boldsymbol{\kappa} + \mathbf{M}(\tau_{\text{eq}} - \tau_{\text{y}}^0) - \boldsymbol{\sigma}_{\text{c}}$, *i.e.*

$$\Phi_{\text{n}} = \max \text{eig} \left[\boldsymbol{\kappa} + \mathbf{M}(\tau_{\text{eq}} - \tau_{\text{y}}^0) - \boldsymbol{\sigma}_{\text{c}} \right] \geq 0 \,. \tag{27}$$

For an isotropic case (isotropic matrix and spherical inclusions), $\mathbf{M} = M\mathbf{I}$ and $\boldsymbol{\sigma}_{\text{c}} = \sigma_{\text{c}}\mathbf{I}$, and Eq. (27) degenerates into Eq. (24).

In Eq. (26), $\mathbf{M}$ and $\boldsymbol{\sigma}_{\text{c}}$ are written in the current configuration. Assuming no effect of the plastic flow, these tensors are then obtained from their equivalent forms in the initial configuration through the rotation tensor $\mathbf{R}^{\text{e}}$ computed from the polar decomposition of the elastic part of the deformation gradient $\mathbf{F}^{\text{e}}$ (*i.e.* $\mathbf{R}^{\text{e}} = \mathbf{F}^{\text{e}} \cdot \left(\sqrt{\mathbf{C}^{\text{e}}} \right)^{-1}$), with

$$\mathbf{M} = \mathbf{R}^{\text{e}} \cdot \mathbf{M}_0 \cdot \mathbf{R}^{\text{e}T} \text{ and } \boldsymbol{\sigma}_{\text{c}} = \mathbf{R}^{\text{e}} \cdot \boldsymbol{\sigma}_{\text{c0}} \cdot \mathbf{R}^{\text{e}T} \,, \tag{28}$$

where $\mathbf{M}_0$ and $\boldsymbol{\sigma}_{\text{c0}}$ are material constants. For an ellipsoidal inclusion whose longitudinal axis is $\mathbf{n}_{\text{long}}$, $\mathbf{M}_0$ and $\boldsymbol{\sigma}_{\text{c0}}$ take the form

$$\mathbf{M}_0 = M_{\text{L}} \mathbf{n}_{\text{long}} \otimes \mathbf{n}_{\text{long}} + M_{\text{T}} \left(\mathbf{I} - \mathbf{n}_{\text{long}} \otimes \mathbf{n}_{\text{long}} \right) \text{, and} \tag{29}$$

$$\boldsymbol{\sigma}_{\text{c0}} = \sigma_{\text{cL}} \mathbf{n}_{\text{long}} \otimes \mathbf{n}_{\text{long}} + \sigma_{\text{cT}} \left(\mathbf{I} - \mathbf{n}_{\text{long}} \otimes \mathbf{n}_{\text{long}} \right) \,, \tag{30}$$

where M_{L}, M_{T}, σ_{cL} and σ_{cT} are material constants. The constraint σ_{cL} can be interpreted as the fracture stress of the MnS inclusion with void nucleation occurring by particle breaking when pulled along the main particle axis and σ_{cT} as the interface decohesion stress which preferentially occurs when the main loading direction is transverse to the main particle axis.

5.3. Model summary

The material parameters of the GTN model enriched with the anisotropic nucleation model described in Section 5.2 consist of the elastoplastic parameters summarized in Tab. 2 and of the porosity-related parameters summarized in Tab. 3. In general, the identification of a parameter of such a material model can be performed either by experimental characterization [30] or by inverse modeling based on mechanical tests [53, 54] depending on its physical meaning. The first approach allows calibrating a material parameter in a more physical way. In the latter, a material law is considered as phenomenological and involves fitting parameters; the results obtained by numerical simulations are then fitted to the experimental ones such that the material parameters can be found with a suitable optimization algorithm.

5.4. Identification and validation of void nucleation law

The determination of the void nucleation law described in Section 5.2 is inspired from the work of [10, 55]. In particular, effective values of the porosity are defined based on the void nucleation mechanism. These effective porosity values are not the voids physically measured, but are values that can be used within the GTN model (which, again, does not take void shape into account explicitly) to properly account for the configuration of the voids associated to the specific void nucleation mode.

The values of the effective nucleated porosity f_{nL} and f_{nT} required in Eq. (23) are identified first. On the one hand, as discussed before, when the inclusions are loaded under

Table 3: Porosity-related parameters of the GTN model enriched with the anisotropic nucleation model.

q_1, q_2	GTN coefficients (see Eq. (17))
f_{V0}	Initial porosity
k_ω	Shear-controled void growth factor (see Eq. (19))
s_{N}, p_{N}	Nucleation intensity parameters (see Eq. (22))
f_{nL}, f_{nT}	Longitudinal and transverse nucleated porosity (see Eq. (23))
M_{L}, M_{T}	Nucleation activation parameters (see Eq. (29))
σ_{cL}, σ_{cT}	Nucleation activation parameters (see Eq. (30))

their main axis, voids nucleate by inclusion cracking. In the case of elongated inclusions with volumetric fraction f_{incl} and initial aspect ratio $W_{0\mathrm{L}}$ (so-called longitudinal aspect ratio), penny-shaped voids are generated with a very small aspect ratio $W_{\mathrm{nucl}} \ll 1$, see the schematics of Fig. 12a. Following [10], for a sufficiently low particle fraction (*i.e.* $f_{\mathrm{incl}} < 2\%$), an effective "spherical" porosity f_{n} can be evaluated by

$$f_{\mathrm{nL}} = \frac{f_{\mathrm{incl}}}{W_{0\mathrm{L}}} \,. \tag{31}$$

If an inclusion breaks into $n+1$ fragments, Eq. (31) becomes

$$f_{\mathrm{nL}} = n\frac{f_{\mathrm{incl}}}{W_{0\mathrm{L}}} \,. \tag{32}$$

On the other hand, when the inclusions are loaded along the transverse direction, voids nucleate by inclusion/matrix decohesion resulting in one large void only, see the schematics of Fig. 12b. As a result, Eq. (31) is reconsidered in the form

$$f_{\mathrm{nT}} = \frac{f_{\mathrm{incl}}}{W_{0\mathrm{T}}} \,, \tag{33}$$

where $W_{0\mathrm{T}}$ is the transverse aspect ratio.

For an ellipsoidal inclusion with semi-axes R_{L} and R_{T}, one has $W_{0\mathrm{L}} = R_{\mathrm{L}}/R_{\mathrm{T}}$ and

$$W_{0\mathrm{T}} = \frac{R_{\mathrm{T}}}{\sqrt{R_{\mathrm{T}}R_{\mathrm{L}}}} = \frac{1}{\sqrt{W_{0\mathrm{L}}}} \,. \tag{34}$$

Based on the microstructure characterization performed in Section 2.1, the following values are selected $W_{0\mathrm{L}} = 24$ and $W_{0\mathrm{T}} = 0.204$. Furthermore, the micrographs show that inclusions break into multiple small equiaxed fragments. A longer particle leads to a higher number of fragments. For simplicity, it is assumed that $f_{\mathrm{nL}} \approx f_{\mathrm{incl}}$. With $f_{\mathrm{incl}} = 2 \times 10^{-3}$, leading to the effective porosity values to be nucleated $f_{\mathrm{nL}} \approx 2 \times 10^{-3}$ and $f_{\mathrm{nT}} \approx 9.8 \times 10^{-3}$.

The remaining parameters to calibrate are the concentration factor $\mathbf{M}_0$ and the critical stress $\boldsymbol{\sigma}_{\mathrm{c}0}$ following the expressions respectively given by Eq. (29) and Eq. (30). As the MnS inclusions have a very low material integrity with the matrix, which induces void nucleation immediately at the onset of yielding, one considers $\sigma_{\mathrm{cL}} = \sigma_{\mathrm{cT}} = \tau_{\mathrm{y}}^0$. For the concentration factor $\mathbf{M}_0$, the values of M_{T} and M_{L} are estimated based on the inclusions geometry characterized in Section 2.1 and using the relationship provided in [12]. One finally obtains

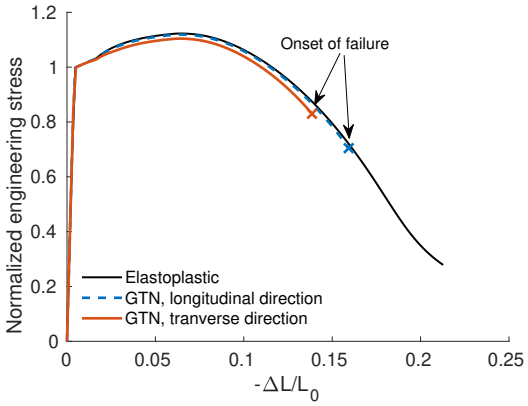

Figure 18: Comparison of the engineering stress/engineering strain response obtained with the elastoplastic model and with the GTN model in the longitudinal and transverse directions.

$M_{\mathrm{T}} = 5.35$ and $M_{\mathrm{L}} = 18.8$. Additionally, in Eq. (22), $s_{\mathrm{N}} = 5 \times 10^{-3}$ and $p_{\mathrm{N}} = 3s_{\mathrm{N}}$ are used to ensure that the end of the void nucleation process occurs at a relatively small plastic strain and that the integral of the truncated Gaussian distribution is close to the integral of the real Gaussian distribution. The parameters for the anisotropic nucleation law are summarized in Table 4.

Table 4: The anisotropic nucleation parameters.

s_{N}	p_{N}	f_{nL}	f_{nT}
5×10^{-3}	15×10^{-3}	2×10^{-3}	9.8×10^{-3}
M_{L}	M_{T}	$\sigma_{\mathrm{cL}}/\tau_{\mathrm{y}}^0$	$\sigma_{\mathrm{cT}}/\tau_{\mathrm{y}}^0$
18.8	5.35	1	1

The material parameters required for the GTN model described in Section 5.1 consist of the elastoplastic parameters reported in Tab. 2, the parameters of the void nucleation law reported in Tab. 4, and the remaining porosity-related parameters including q_1, q_2, k_ω, and f_{V0}. The material is assumed to be initially intact with $f_{V0} = 0$ and the porosity originates thus only from the void nucleation on the MnS inclusions. Since the Nahshon-Hutchinson shear term $\dot{f}_{V\,\mathrm{sh}}$ in Eq. (19) vanishes for axisymmetric stress states whatever the value of k_ω, we consider a value $k_\omega = 0$ for this particular test. The values of $q_1 = 1.414$ and $q_2 = 1$ were identified based on the void cell simulations reported in Part II of this work [45].

Figure 18 compares, for the SRB specimens, the elastoplastic prediction obtained in Section 4 to the predictions obtained with the GTN model for both the longitudinal and transverse directions. Since void coalescence is not considered within this GTN model –it will be captured in the framework of the coupled GTN/Thomason model in Part II– the predictions of the GTN model shown in Fig. 18 are truncated at the onset of fracture identified by the experimental values in the corresponding experimental tests. Prior to the onset of failure, the elastoplastic and GTN models yield close results as a result of the relatively low porosity level, see also [56]. However, the GTN model allows predicting the void distribution resulting from the void growth phase, which is extracted along the axisymmetric axis and compared to the experimental measurements in Fig. 19.

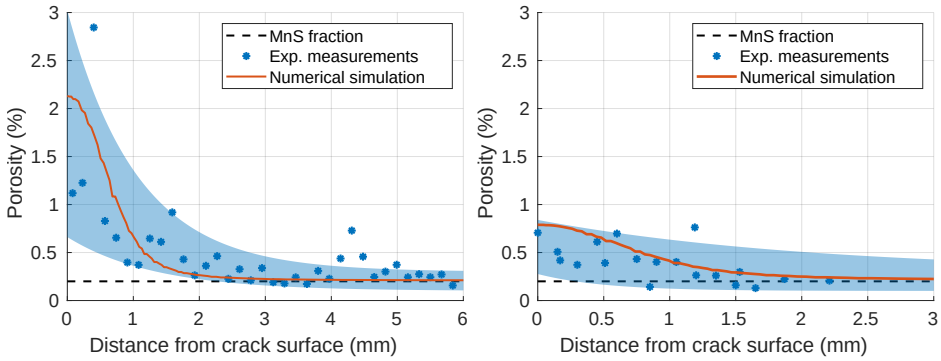

Figure 19: Comparison of the apparent porosity distributions in terms of the distance to the fracture surface obtained with the numerical simulations on the SRB specimens and the experimental measurements of the fraction of MnS inclusions contributing to void nucleation: (a) in the longitudinal direction (in this case the apparent porosity distribution is $\approx f_V$), and (b) in the transverse direction (in this case the apparent porosity distribution is $\approx f_V/\sqrt{W_{0\mathrm{L}}}$).

Because void shape effects are heuristically accounted for through Eqs. (32, 33), the apparent porosity in the longitudinal direction is equivalent to the effective porosity f_V, while the apparent porosity in the transverse direction is estimated by $f_V/\sqrt{W_{0\mathrm{L}}}$. Figure 19 reports the apparent porosity distributions predicted with the numerical simulations using the GTN model compared to the experimental measurement described in Section 3.2. The numerical distributions are consistent with the experimental data in both directions despite the high data dispersion. This gives confidence in the proposed void nucleation law even though only the full validation addressed in Part II, involving the prediction of the fracture strain, will provide a definitive assessment of the model.

The void nucleation law sensibility to its material parameters is now investigated by studying their effects on the distribution of the apparent porosity as illustrated in Fig. 20 for the SRB specimen loaded in the longitudinal direction. As expected, the value of W_{0L} has a strong effect as reported in Fig. 20a. The results are not very sensitive to the values of σ_{cL} as shown in Fig. 20b. This last observation is explained by Eq. (27) in which the term in $\mathbf{M}$ rapidly increases during the void growth phase, leading to satisfying the condition (27) at small plastic deformation despite a high value of σ_{cL}. Since the value of s_{N} determines the range of plastic strains in which the complete void nucleation occurs, this parameter has almost no effect providing it remains small enough as shown in Fig. 20c.

6. Conclusions

The ductile fracture behavior of a high strength steel has been experimentally investigated under different stress states using cylindrical round bars, plane strain, and plane stress specimens. Owing to the presence of notches, a wide range of stress triaxiality and Lode parameter values has been covered. The elastoplastic properties and void nucleation have been analyzed in details. The main contributions of the work are the followings:

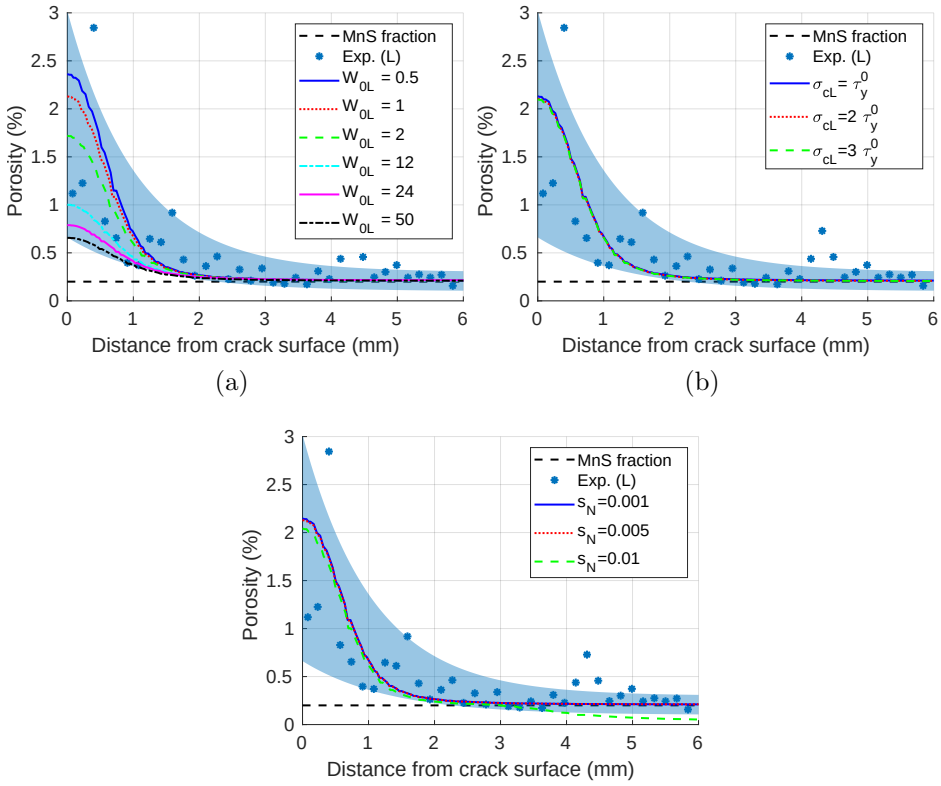

Figure 20: Distribution of the apparent porosity in terms of the distance to the fracture surface for the L-SRB specimen simulations conducted with different parameters of the void nucleation law: (a) effect of W_{0T}, (b) effect of σ_{cL}, and (c) effect of s_{N}; the experimental measurements and the fraction of MnS inclusions contributing to void nucleation are also reported.

- A strong anisotropy on the fracture strain is found, resulting from the morphological anisotropy of the MnS inclusions, but with no significant plastic anisotropy.
- An anisotropic void nucleation law has been developed in the context of the GTN model to capture the fracture anisotropy. The model involves two void nucleation mechanisms: particle cracking and matrix/particle decohesion. Testing specimens extracted along orientations other than the transverse and longitudinal ones would allow checking the validity of the model for such a difficult case that would involve void rotation, an effect not directly taken into account in the current formulation.

In Part II of this work [45], the material parameters calibration for the GTN model enhanced by the Nahshon-Hutchinson shear modification in combination with the Thomason model will be conducted based on the same set of experimental data. The damage-to-crack transition framework developed in [39] will be considered to model the crack propagation and validate the numerical method.

Acknowledgments

The research has been funded by the Walloon Region under the agreement no.7581-MRIPF in the context of the 16th MECATECH call.

Data availability

Due to the confidential nature of the research project, participants of this study did not agree for their data to be shared publicly, so supporting data is not available.

References

[1] A. A. Benzerga, J.-B. Leblond, Ductile fracture by void growth to coalescence, in: H. Aref, E. van der Giessen (Eds.), Advances in Applied Mechanics, Vol. 44 of Advances in Applied Mechanics, Elsevier, 2010, pp. 169 – 305 (2010). doi:https://doi.org/10.1016/S0065-2156(10)44003-X.
URL http://www.sciencedirect.com/science/article/pii/S006521561044003X

[2] A. A. Benzerga, J.-B. Leblond, A. Needleman, V. Tvergaard, Ductile failure modeling, International Journal of Fracture 201 (1) (2016) 29–80 (Sep 2016). doi:10.1007/s10704-016-0142-6.
URL https://doi.org/10.1007/s10704-016-0142-6

[3] A. Pineau, A. Benzerga, T. Pardoen, Failure of metals i: Brittle and ductile fracture, Acta Materialia 107 (2016) 424 – 483 (2016). doi:https://doi.org/10.1016/j.actamat.2015.12.034.
URL http://www.sciencedirect.com/science/article/pii/S1359645415301403

[4] S. Goods, L. Brown, Overview no. 1: The nucleation of cavities by plastic deformation, Acta Metallurgica 27 (1) (1979) 1 – 15 (1979). doi:https://doi.org/10.1016/0001-6160(79)90051-8.
URL http://www.sciencedirect.com/science/article/pii/0001616079900518

[5] A. Pineau, Review of fracture micromechanisms and a local approach to predicting crack resistance in low strength steels, Advances in Fracture Mechanics Research, ICF5, 1982 (1982) 553–577 (1982).

[6] F. Montheillet, F. Moussy, Physique et mécanique de l'endommagement, les Ed. de Physique, 1986 (1986).

[7] A. Pineau, T. Pardoen, Failure mechanisms of metals, Comprehensive structural integrity encyclopedia 2 (2007) 684–797 (2007).

[8] L. Babout, Y. Brechet, E. Maire, R. Fougres, On the competition between particle fracture and particle decohesion in metal matrix composites, Acta Materialia 52 (15) (2004) 4517 – 4525 (2004). doi:https://doi.org/10.1016/j.actamat.2004.06.009.
URL http://www.sciencedirect.com/science/article/pii/S1359645404003477

[9] C. Chu, A. Needleman, Void nucleation effects in biaxially stretched sheets, Journal of engineering materials and technology 102 (3) (1980) 249–256 (1980).

[10] D. Lassance, F. Scheyvaerts, T. Pardoen, Growth and coalescence of penny-shaped voids in metallic alloys, Engineering Fracture Mechanics 73 (8) (2006) 1009–1034 (2006). doi:10.1016/j.engfracmech.2005.12.004.
URL https://linkinghub.elsevier.com/retrieve/pii/S0013794405003048

[11] G. Huber, Y. Brechet, T. Pardoen, Predictive model for void nucleation and void growth controlled ductility in quasi-eutectic cast aluminium alloys, Acta Materialia 53 (9) (2005) 2739 – 2749 (2005). doi:https://doi.org/10.1016/j.actamat.2005.02.037.
URL http://www.sciencedirect.com/science/article/pii/S1359645405001357

[12] F. Beremin, Cavity formation from inclusions in ductile fracture of a508 steel, Metallurgical Transactions A 12 (5) (1981) 723–731 (1981).

[13] T. Pardoen, J. Hutchinson, An extended model for void growth and coalescence, Journal of the Mechanics and Physics of Solids 48 (12) (2000) 2467 – 2512 (2000). doi:https://doi.org/10.1016/S0022-5096(00)00019-3.
URL http://www.sciencedirect.com/science/article/pii/S0022509600000193

[14] I. Barsoum, J. Faleskog, Rupture mechanisms in combined tension and shearexperiments, International Journal of Solids and Structures 44 (6) (2007) 1768 – 1786, physics and Mechanics of Advanced Materials (2007). doi:https://doi.org/10.1016/j.ijsolstr.2006.09.031.
URL http://www.sciencedirect.com/science/article/pii/S0020768306003921

[15] Y. Bai, T. Wierzbicki, A new model of metal plasticity and fracture with pressure and lode dependence, International Journal of Plasticity 24 (6) (2008) 1071 – 1096 (2008). doi:https://doi.org/10.1016/j.ijplas.2007.09.004.
URL http://www.sciencedirect.com/science/article/pii/S0749641907001246

[16] K. Nahshon, J. Hutchinson, Modification of the gurson model for shear failure, European Journal of Mechanics - A/Solids 27 (1) (2008) 1 – 17 (2008). doi:https://doi.org/10.1016/j.euromechsol.2007.08.002.
URL http://www.sciencedirect.com/science/article/pii/S0997753807000721

[17] L. Xue, Constitutive modeling of void shearing effect in ductile fracture of porous materials, Engineering Fracture Mechanics 75 (11) (2008) 3343 – 3366, local Approach to Fracture (19862006): Selected papers from the 9th European Mechanics of Materials Conference (2008). doi:https://doi.org/10.1016/j.engfracmech.2007.07.022.
URL http://www.sciencedirect.com/science/article/pii/S0013794407003220

[18] X. Gao, T. Zhang, J. Zhou, S. M. Graham, M. Hayden, C. Roe, On stress-state dependent plasticity modeling: Significance of the hydrostatic stress, the third invariant of stress deviator and the non-associated flow rule, International Journal of Plasticity 27 (2) (2011) 217–231 (2011). doi:10.1016/j.ijplas.2010.05.004.
URL http://dx.doi.org/10.1016/j.ijplas.2010.05.004

[19] I. Barsoum, J. Faleskog, S. Pingle, The effect of stress state on ductility in the moderate stress triaxiality regime of medium and high strength steels, International Journal of Mechanical Sciences 65 (1) (2012) 203 – 212 (2012). doi:https://doi.org/10.1016/j.ijmecsci.2012.10.003.
URL http://www.sciencedirect.com/science/article/pii/S0020740312002226

[20] J. Faleskog, I. Barsoum, Tensiontorsion fracture experimentspart i: Experiments and a procedure to evaluate the equivalent plastic strain, International Journal of Solids and Structures 50 (25) (2013) 4241 – 4257 (2013). doi:https://doi.org/10.1016/j.ijsolstr.2013.08.029.
URL http://www.sciencedirect.com/science/article/pii/S0020768313003454

[21] M. Achouri, G. Germain, P. D. Santo, D. Saidane, Experimental characterization and numerical modeling of micromechanical damage under different stress states, Materials & Design 50 (2013) 207 – 222 (2013). doi:https://doi.org/10.1016/j.matdes.2013.02.075.
URL http://www.sciencedirect.com/science/article/pii/S0261306913001866

[22] M. Dunand, D. Mohr, Effect of lode parameter on plastic flow localization after proportional loading at low stress triaxialities, Journal of the Mechanics and Physics of Solids 66 (2014) 133 – 153 (2014). doi:https://doi.org/10.1016/j.jmps.2014.01.008.
URL http://www.sciencedirect.com/science/article/pii/S0022509614000180

[23] Y. Zhu, M. D. Engelhardt, R. Kiran, Combined effects of triaxiality, lode parameter and shear stress on void growth and coalescence, Engineering Fracture Mechanics 199 (2018) 410 – 437 (2018). doi:https://doi.org/10.1016/j.engfracmech.2018.06.008.
URL http://www.sciencedirect.com/science/article/pii/S0013794418300766

[24] V.-D. Nguyen, T. Pardoen, L. Noels, A nonlocal approach of ductile failure incorporating void growth, internal necking, and shear dominated coalescence mechanisms, Journal of

the Mechanics and Physics of Solids 137 (2020) 103891 (2020). doi:https://doi.org/10.1016/j.jmps.2020.103891.
URL http://www.sciencedirect.com/science/article/pii/S0022509619309275

[25] A. L. Gurson, Continuum theory of ductile rupture by void nucleation and growth: Part i - yield criteria and flow rules for porous ductile media, Journal of Engineering Materials and Technology 99 (1) (1977) 2–15 (1977).

[26] V. Tvergaard, A. Needleman, Analysis of the cup-cone fracture in a round tensile bar, Acta Metallurgica 32 (1) (1984) 157 – 169 (1984). doi:https://doi.org/10.1016/0001-6160(84)90213-X.
URL http://www.sciencedirect.com/science/article/pii/000161608490213X

[27] A. Needleman, V. Tvergaard, An analysis of ductile rupture in notched bars, Journal of the Mechanics and Physics of Solids 32 (6) (1984) 461 – 490 (1984). doi:https://doi.org/10.1016/0022-5096(84)90031-0.
URL http://www.sciencedirect.com/science/article/pii/0022509684900310

[28] M. Gologanu, J.-B. Leblond, J. Devaux, Approximate models for ductile metals containing non-spherical voids - case of axisymmetric prolate ellipsoidal cavities, Journal of the Mechanics and Physics of Solids 41 (11) (1993) 1723 – 1754 (1993). doi:https://doi.org/10.1016/0022-5096(93)90029-F.
URL http://www.sciencedirect.com/science/article/pii/002250969390029F

[29] M. Gologanu, J.-B. Leblond, J. Devaux, Approximate models for ductile metals containing nonspherical voids - case of axisymmetric oblate ellipsoidal cavities, Journal of Engineering Materials and Technology 116 (3) (1994) 290–297 (1994).

[30] T. Pardoen, Numerical simulation of low stress triaxiality ductile fracture, Computers & Structures 84 (26) (2006) 1641 – 1650 (2006). doi:https://doi.org/10.1016/j.compstruc.2006.05.001.
URL http://www.sciencedirect.com/science/article/pii/S0045794906001659

[31] P. Thomason, A three-dimensional model for ductile fracture by the growth and coalescence of microvoids, Acta Metallurgica 33 (6) (1985) 1087 – 1095 (1985). doi:https://doi.org/10.1016/0001-6160(85)90202-0.
URL http://www.sciencedirect.com/science/article/pii/0001616085902020

[32] P. Thomason, Three-dimensional models for the plastic limit-loads at incipient failure of the intervoid matrix in ductile porous solids, Acta Metallurgica 33 (6) (1985) 1079 – 1085 (1985). doi:https://doi.org/10.1016/0001-6160(85)90201-9.
URL http://www.sciencedirect.com/science/article/pii/0001616085902019

[33] A. Benzerga, Micromechanics of coalescence in ductile fracture, Journal of the Mechanics and Physics of Solids 50 (6) (2002) 1331 – 1362 (2002). doi:https://doi.org/10.1016/S0022-5096(01)00125-9.
URL http://www.sciencedirect.com/science/article/pii/S0022509601001259

[34] F. Scheyvaerts, T. Pardoen, P. Onck, A new model for void coalescence by internal necking, International Journal of Damage Mechanics 19 (1) (2010) 95–126 (2010). arXiv:https://doi.org/10.1177/1056789508101918, doi:10.1177/1056789508101918.
URL https://doi.org/10.1177/1056789508101918

[35] A. A. Benzerga, J.-B. Leblond, Effective yield criterion accounting for microvoid coalescence, Journal of Applied Mechanics 81 (3) (2014) 031009 (2014).

[36] Z. Zhang, C. Thaulow, J. degrd, A complete gurson model approach for ductile fracture, Engineering Fracture Mechanics 67 (2) (2000) 155 – 168 (2000). doi:https://doi.org/10.1016/S0013-7944(00)00055-2.
URL http://www.sciencedirect.com/science/article/pii/S0013794400000552

[37] A. A. Benzerga, J. Besson, R. Batisse, A. Pineau, Synergistic effects of plastic anisotropy and void coalescence on fracture mode in plane strain, Modelling and Simulation in Materials Science and Engineering 10 (1) (2002) 73 (2002).
URL http://stacks.iop.org/0965-0393/10/i=1/a=306

[38] J. Besson, Damage of ductile materials deforming under multiple plastic or viscoplastic mechanisms, International Journal of Plasticity 25 (11) (2009) 2204 – 2221 (2009). doi:https://doi.org/10.1016/j.ijplas.2009.03.001.
URL http://www.sciencedirect.com/science/article/pii/S0749641909000357

[39] J. Leclerc, V.-D. Nguyen, T. Pardoen, L. Noels, A micromechanics-based non-local damage to crack transition framework for porous elastoplastic solids, International Journal of Plasticity 127 (2020) 102631 (2020). doi:https://doi.org/10.1016/j.ijplas.2019.11.010.
URL http://www.sciencedirect.com/science/article/pii/S0749641919303821

[40] R. De Borst, L. Sluys, H.-B. Muhlhaus, J. Pamin, Fundamental issues in finite element analyses of localization of deformation, Engineering computations 10 (2) (1993) 99–121 (1993).

[41] R. H. J. Peerlings, R. De Borst, W. A. M. Brekelmans, J. H. P. De Vree, Gradient enhanced damage for quasi-brittle materials, International Journal for Numerical Methods in Engineering 39 (19) (1996) 3391–3403 (1996).
URL http://www.scopus.com/inward/record.url?eid=2-s2.0-0030267284&partnerID=tZOtx3y1

[42] P. Håkansson, M. Wallin, M. Ristinmaa, Thermomechanical response of non-local porous material, International Journal of Plasticity 22 (11) (2006) 2066 – 2090, damage and Fracture: Modeling and Experiments (2006). doi:https://doi.org/10.1016/j.ijplas.2005.08.003.
URL http://www.sciencedirect.com/science/article/pii/S0749641906000623

[43] F. Reusch, C. Hortig, B. Svendsen, Nonlocal modeling and simulation of ductile damage and failure in metal matrix composites, Journal of Engineering Materials and Technology 130 (2) (2008) 021009 (2008).

[44] G. Hütter, T. Linse, S. Roth, U. Mühlich, M. Kuna, A modeling approach for the complete ductile–brittle transition region: cohesive zone in combination with a nonlocal gurson-model, International Journal of Fracture 185 (1) (2014) 129–153 (Jan 2014). doi:10.1007/s10704-013-9914-4.
URL https://doi.org/10.1007/s10704-013-9914-4

[45] J. Leclerc, M. Marteleur, M.-S. Colla, T. Pardoen, L. Noels, V.-D. Nguyen, Ductile fracture of high strength steels with morphological anisotropy. part ii: Nonlocal micromechanics-based modeling (In Preparation).

[46] L. E. Dæhli, D. Morin, T. Børvik, O. S. Hopperstad, A lode-dependent gurson model motivated by unit cell analyses, Engineering Fracture Mechanics 190 (2018) 299 – 318 (2018). doi:https://doi.org/10.1016/j.engfracmech.2017.12.023.
URL http://www.sciencedirect.com/science/article/pii/S0013794417306872

[47] F. Hannard, T. Pardoen, E. Maire, C. Le Bourlot, R. Mokso, A. Simar, Characterization and micromechanical modelling of microstructural heterogeneity effects on ductile fracture of 6xxx aluminium alloys, Acta Materialia 103 (2016) 558–572 (2016). doi:10.1016/j.actamat.2015.10.008.
URL https://linkinghub.elsevier.com/retrieve/pii/S1359645415300094

[48] Y. Bai, Effect of loading history on necking and fracture, PhD. Massachusetts Institute of Technology, Cambridge, USA (2007).

[49] A. L. Eterovic, K.-J. Bathe, A hyperelastic-based large strain elasto-plastic constitutive formulation with combined isotropic-kinematic hardening using the logarithmic stress and strain measures, International Journal for Numerical Methods in Engineering 30 (6) (1990) 1099–1114 (1990). arXiv:https://onlinelibrary.wiley.com/doi/pdf/10.1002/nme.1620300602, doi:10.1002/nme.1620300602.
URL https://onlinelibrary.wiley.com/doi/abs/10.1002/nme.1620300602

[50] M. E. Gurtin, L. Anand, The decomposition f=fefp, material symmetry, and plastic irrotationality for solids that are isotropic-viscoplastic or amorphous, International Journal of Plasticity 21 (9) (2005) 1686 – 1719 (2005). doi:https://doi.org/10.1016/j.ijplas.2004.11.007.
URL http://www.sciencedirect.com/science/article/pii/S0749641904001603

[51] A. Cuitino, M. Ortiz, A material-independent method for extending stress update algorithms from small-strain plasticity to finite plasticity with multiplicative kinematics, Engineering computations 9 (1992) 437–437 (1992).

[52] J. Leclerc, V.-D. Nguyen, T. Pardoen, L. Noels, A micromechanics-based non-local damage to crack transition framework for porous elastoplastic solids, International Journal of Plasticity (2020). doi:10.1016/j.ijplas.2019.11.010.

[53] Z. Xue, M. Pontin, F. Zok, J. Hutchinson, Calibration procedures for a computational model of ductile fracture, Engineering Fracture Mechanics 77 (3) (2010) 492 – 509 (2010).

doi:https://doi.org/10.1016/j.engfracmech.2009.10.007.
URL http://www.sciencedirect.com/science/article/pii/S0013794409003233

[54] M. Dunand, D. Mohr, On the predictive capabilities of the shear modified gurson and the modified mohrcoulomb fracture models over a wide range of stress triaxialities and lode angles, Journal of the Mechanics and Physics of Solids 59 (7) (2011) 1374 – 1394 (2011). doi:https://doi.org/10.1016/j.jmps.2011.04.006.
URL http://www.sciencedirect.com/science/article/pii/S0022509611000688

[55] D. Lassance, D. Fabregue, F. Delannay, T. Pardoen, Micromechanics of room and high temperature fracture in 6xxx Al alloys, Progress in Materials Science 52 (1) (2007) 62–129 (2007). doi:10.1016/j.pmatsci.2006.06.001.
URL https://linkinghub.elsevier.com/retrieve/pii/S0079642506000399

[56] T. Pardoen, F. Delannay, Assessment of void growth models from porosity measurements in cold-drawn copper bars, Metallurgical and Materials Transactions A 29 (7) (1998) 1895–1909 (Jul. 1998). doi:10.1007/s11661-998-0014-4.